UNIVERSITY OF LATVIA

Summary of Doctoral Thesis

Margarita Baitimirova

FABRICATION OF GRAPHENE CONTAINING LAYERED NANOSTRUCTURES AND INVESTIGATION OF THEIR PROPERTIES

Riga, 2022

UNIVERSITY OF LATVIA

Faculty of Chemistry
Institute of Chemical Physics

Margarita Baitimirova

FABRICATION OF GRAPHENE CONTAINING LAYERED NANOSTRUCTURES AND INVESTIGATION OF THEIR PROPERTIES

Summary of Doctoral Thesis

Submitted for the degree of Doctor of Chemistry
Subfield of Physical Chemistry

Riga, 2022

The doctoral thesis was carried out at the Chair of Institute of Chemical Physics, University of Latvia from 2014 to 2022.

This work has been developed with the support of the ESF project "Strengthening of the capacity of doctoral studies at the University of Latvia within the framework of the new doctoral model" no. 8.2.2.0/20/I/006 (2021-2023), ERAF project "Thermoelectric nanomaterials/topological insulators for more effective waste heat converting to usable energy" No. 1.1.1.1/16/A/257 (2017-2020), Latvia-France cooperation project "OSMOSIS. ALD on graphene for optical biosensors applications" (2016-2017) and the support of the Latvian State research program "IMIS-2 Multifunctional materials and composites, photonics and nanotechnology" (2014-2017).

The thesis contains the Introduction, 3 Chapters, Conclusions and the Reference list.

Form of the thesis: dissertation in the Chemistry sector, Physical Chemistry subsector.

Supervisor: *Prof., Dr. chem.* Donāts Erts

Reviewers:

Assoc. prof., Dr. chem. Agris Bērziņš (University of Latvia)
Prof., Dr. sc. ing. Andris Šutka (Riga Technical University)
Prof., PhD Justin D. Holmes (University College Cork)

The thesis will be defended in a public session of the Doctoral Committee of Chemistry, University of Latvia at 15:00 on November 4, 2022 at the Faculty of Chemistry of University of Latvia, Jelgavas str. 1, auditorium 108, Riga.

The thesis and the summary of the thesis are available at the Library of the University of Latvia, Raiņa blvd. 19.

Chairman of the Doctoral Committee — *prof.* E. Sūna
Secretary of the Doctoral Committee — *assoc. prof.* V. Rudoviča

ISBN 978-9934-18-876-3
ISBN 978-9934-18-877-0 (PDF)

ABSTRACT

The doctoral thesis is dedicated to the fabrication of new layered nanomaterials with improved structure, optical and thermoelectric properties, and to testing of these nanomaterials for applications in electronic, thermoelectric and photosensitive devices. The fabricated nanomaterials are based on the unique carbon allotrope – graphene – joined together with the well-known thermoelectric and/or optically active materials such as bismuth selenide and zinc oxide.

In this work, methodologies for the synthesis of individual nanostructures and nanostructured coatings of bismuth selenide on different surfaces (glass, quartz, graphene, indium-tin-oxide, anodized aluminum oxide) are developed. A prototype of a thermoelectric device based on bismuth selenide nanostructured coating enclosed between two graphene layers is demonstrated. Graphene/zinc oxide nanolaminates with a different number of graphene layers and zinc oxide interlayers with different thicknesses are fabricated for the first time. The crystalline and optical properties of these structures in relation to the number of graphene interlayers and thickness of zinc oxide layers are investigated, which is important for their prospective applications in optical sensors and optoelectronic devices. Bismuth selenide/zinc oxide layered heterostructures on graphene substrate are synthesized, the impact of the graphene substrate on the structure and optical properties of the zinc oxide layer is investigated. The charge transfer processes that occur in graphene-containing layered nanostructures and are responsible for the improvement of the optical and thermoelectric properties of these structures are clarified.

GRAPHENE, BISMUTH SELENIDE, ZINC OXIDE, LAYERED NANOSTRUCTURES, NANOLAMINATES, PHYSICAL VAPOR DEPOSITION, THERMOELECTRIC, PHOTOLUMINESCENCE

CONTENTS

INTRODUCTION

In the last years, reducing waste heat and obtaining energy from renewable resources are more and more relevant. One of the solutions to such tasks is the application of thermoelectric (TE) devices to convert waste heat into electricity. Bismuth selenide (Bi_2Se_3) is a promising material for the use in TE devices due to its effective thermoelectric properties at near-room temperatures [1]. One of the ways to improve the TE properties of a material is to reduce its dimensions to the nanometer scale, or to make it nanostructured. As a result of nanostructuring, the surface-to-volume ratio of the material increases, grain sizes and defect concentrations changes. That significantly affects the TE properties of the materials. In addition, the reduction of the Bi_2Se_3 dimensions to the nanometer scale reveals its topological insulator properties [2], which is important for applications in electronic, spintronic and quantum computing devices. The high elastic modulus and low resistivity of Bi_2Se_3 make it a promising material for applications in nanoelectromechanical switches [3].

One of the ways to reduce the dimensions of the material is to synthesize the thin films, nanostructured coatings, nanoplates and nanoribbons on different surfaces. Nanostructured Bi_2Se_3 can be obtained by molecular beam epitaxy (MBE), physical vapor deposition (PVD), thermal evaporation, etc. Among these methods, PVD is the simplest and cheapest method. However, the substrate type has an important influence on nanostructure synthesis by this PVD method. The surface properties of the substrate can influence the morphology and, respectively, physical properties of the deposited nanostructures. Therefore, it is important to study the growth mechanism of Bi_2Se_3 nanostructures on different substrates.

Graphene is a promising material to be used as a substrate for the synthesis of Bi_2Se_3 nanostructured coatings. Graphene can be obtained by various methods: chemical vapor deposition (CVD) with the subsequent polymer-based transfer, exfoliation, thermal decomposition of SiC substrates, etc. Among these methods, the CVD method has advantages for use it in the fabrication of layered nanostructures due to the ability to obtain large-area monolayer graphene with the possibility to transfer it to the target substrate. Due to the high similarity of graphene and Bi_2Se_3 crystal lattices (the lattice mismatch is ~2.9% [4]), graphene promotes epitaxial (horizontally oriented to the substrate surface) growth of the Bi_2Se_3 nanostructures. Graphene itself can serve as a transparent electrode in such graphene/Bi_2Se_3 structures due to its high electrical and thermal conductivities, mechanical strength, and high transparency to visible light (VIS) and near-infrared (IR) radiation. The replacement of traditional optically transparent electrodes (e.g., indium-tin-oxide (ITO) electrodes) with the graphene monolayer may increase the efficiency of thermoelectric and optoelectric devices. However, as graphene has higher electrical conductivity than Bi_2Se_3, the TE measurements of layered G/Bi_2Se_3 structures must be performed *through-plane*. In this case, Bi_2Se_3 nanostructures oriented at different

angles relative the substrate surface are more effective for TE applications due to a higher effective surface area and reduced grain boundaries, resulting in more effective charge transfer and enhanced TE properties. Obtaining of Bi_2Se_3 nanostructures oriented under different angles on the graphene substrate still remains a challenging task due to mentioned above epitaxial growth of Bi_2Se_3 on it.

The topological insulator properties of nanostructured Bi_2Se_3 can be used to enhance the UV emission of a material such as zinc oxide (ZnO), which is known as semiconductor with strong UV photoluminescence (PL) at room temperature. The recent theoretical studies [5] showed the possibility to enhance optical emission of various emitters by surface plasmon resonance existence on the surface of a topological insulator. However, to the best of our knowledge, the mechanisms of enhancement of optical properties and the correlation between optical and structural properties in topological insulator-ZnO heterostructures have not been studied in detail. Coating the top surface of Bi_2Se_3 nanostructures with a ZnO layer may not only improve the optical properties of ZnO but also protect Bi_2Se_3 nanostructures from the degradation under the influence of environmental moisture and pollution [6].

ZnO thin films can be synthesized by various methods – hydrothermal, magnetron sputtering, CVD, atomic layer deposition (ALD). Among these methods, ALD enables controlled synthesis process at the atomic level, resulting in deposition of high-quality and uniform thin films. The ability to synthesize thin films at low temperatures (60-100°C) offered by ALD is important to prevent the interdiffusion of materials in a layered structure.

Due to the high photosensitivity, chemical stability, biocompatibility and non-toxicity, ZnO finds applications in UV, gas and biological sensors [7]. The sensitivity of ZnO can be enhanced not only by the nanostructuring but also by its combination with carbon-based nanomaterials (for example, with graphene) in composites or hybrid structures [8, 9]. Investigations of single graphene-ZnO interfaces showed that the graphene in ZnO/graphene structures acts as an excellent electron acceptor and transport material of photoinduced excitons, which makes the combination of such materials promising for applications in optoelectric devices and chemical sensors [10, 11]. However, no investigation was carried out about ZnO nanostructures enclosed between two graphene layers or “sandwich”-type multilayer structures (nanolaminates) with the graphene and ZnO interlayers.

The **aim** of this doctoral thesis was to synthesize layered nanostructures containing graphene and various semiconductors (Bi_2Se_3, ZnO), which differ in the morphology, thickness and number of components of the nanostructures; to perform structural characterization of the synthesized layered nanostructures, to determine the effect of various external factors (temperature, UV-Vis-IR radiation, etc.) on their optical, thermoelectric and optoelectric properties, and to test the prospective applications of these nanostructures in self-powered TE and photosensitive devices.

To achieve the aim of this doctoral thesis, the following **tasks** were set:

1. To develop a method for obtaining differing in morphology, thickness and density Bi_2Se_3 nanostructures on different substrates. To study the structural properties of the obtained nanostructures.
2. To develop a method for obtaining Bi_2Se_3 nanostructures of different morphology, orientation to the surface of the substrate, and density per unit area, using graphene as a substrate. To compare the growth mechanisms of the nanostructures on graphene with the growth mechanisms on the other substrates. To evaluate the potential application of graphene/Bi_2Se_3 layered nanostructures in thermoelectric devices and infrared sensors.
3. To use graphene monolayers for the fabrication of multi-layered nanostructures (G/ZnO nanolaminates), to study interaction of graphene with the ZnO layers in the nanolaminate and the influence of the thickness of the ZnO layers on the structure and optical properties of the nanolaminates.
4. Using graphene as a substrate, to synthesize layered Bi_2Se_3/ZnO heterostructures with different thicknesses of ZnO layers and Bi_2Se_3 nanostructures of different orientations relative to the substrate surface. To study the influence of graphene on the structure and optical properties of the upper layers.

Theses to be defended:

1. The variation of the morphology of Bi_2Se_3 nanostructures can be achieved by changing the carrier gas flow during the catalyst-free vapor solid deposition.
2. In nanostructured coatings the Bi_2Se_3 nanostructures oriented at different angles relative to the substrate surface will be more thermoelectrically effective than horizontally oriented nanostructures.
3. Graphene can be used to control the structure and physical properties of individual layers in nanolaminates and multilayer heterostructures.

Novelty, scientific and practical significance of the work:

1. Cheap and simple catalyst-free method for the obtaining of Bi_2Se_3 nanostructured coatings and individual nanostructures on conductive (graphene, ITO) and non-conductive (glass, quartz, anodized aluminum oxide (AAO)) substrates is developed. The developed method allows to synthesise the desired nanostructures in controlled and selective manner for the target field of applications (TE and photosensitive devices, nanoelectromechanical switches or current standards).
2. The pronounced thermoelectric effect is demonstrated for Bi_2Se_3 nanostructured coatings, which consisted from the nanoplates oriented under different angles relative to surface of graphene substrate.

3. The prototype based on Bi_2Se_3 nanostructured coating enclosed between the two graphene layers (G/Bi_2Se_3/G) for applications in the field of TE and IR radiation detection is fabricated.

4. The new nanomaterials - G/ZnO nanolaminates are synthesized for the first time. Their structure and optical properties can be optimized depending on the number of graphene layers and thickness of ZnO interlayers.

5. Bi_2Se_3/ZnO heterostructures with significant improvement of ZnO photoluminescence (PL) are fabricated on a graphene substrate for the first time. Possible mechanisms of enhancement of optical properties of ZnO in Bi_2Se_3/ZnO heterostructures are described.

List of publications:

The thesis is based on the work contained in the following papers

1. **M. Baitimirova**, J. Andzane, R. Viter, B. Fraisse, O. Graniel, M. Bechelany, J. Watt, D. Peckus, S. Tamulevicius, D. Erts. Improved crystalline structure and enhanced photoluminescence ZnO nanolayers in Bi_2Se_3/ZnO heterostructures. *Journal of Physical Chemistry C* **2019**, *123*, 31156-31166, DOI: 10.1021/acs.jpcc.9b08417 *(impact factor = 4.29)*

2. G. Kunakova, R. Meija, J. Andzane, U. Malinovskis, G. Petersons, **M. Baitimirova**, M. Bechelany, T. Bauch, F. Lombardi, D. Erts. Surface structure promoted high-yield growth and magnetotransport properties of Bi_2Se_3 nanoribbons. *Scientific Reports* **2019**, *9*, 11328-11338, DOI: 10.1038/s41598-019-47547-0 *impact factor = 3.998)*

3. J. Andzane, L. Britala, E. Kauranens, A. Neciporenko, **M. Baitimirova**, S. Lara-Avila, S. Kubatkin, M. Bechelany, D. Erts. Effect of graphene substrate type on formation of Bi_2Se_3 nanoplates. *Scientific Reports* **2019**, *9*, 4791-4798, DOI: 10.1038/s41598-019-41178-1 *(impact factor = 3.998)*

4. J. Andzane, K. Buks, M.N. Strakova, M. Zubkins, M. Bechelany, M. Marnauza, **M. Baitimirova**, D. Erts. Structure and doping determined thermoelectric properties of Bi_2Se_3 thin films deposited by vapour-solid technique. *IEEE Transactions on Nanotechnology* **2019**, *18*, 948-954, DOI: 10.1109/TNANO.2019.2939862 *impact factor = 2.196)*

5. J. Andzane, K. Buks, M. Zubkins, M. Bechelany, M. Marnauza, **M. Baitimirova**, D. Erts. Structure-determined thermoelectric properties of Bi_2Se_3 thin films deposited by vapour-solid technique. *Proceedings of the IEEE Conference on Nanotechnology* **2019**, 2018-July, 8626225 *(impact factor = 0.102)*

6. Iatsunskyi, **M. Baitimirova**, E. Coy, L. Yate, R. Viter, A. Ramanavicius, S. Jurga, M. Bechelany, D. Erts. Influence of ZnO/graphene nanolaminate periodicity on their structural and mechanical properties. *Journal of Materials Science & Technology.* **2018**, *34*, 1487-1493, DOI: 10.1016/j.jmst.2018.03.022 *(impact factor = 5.07)*

7. **M. Baitimirova**, R. Viter, J. Andzane, A. van der Lee, D. Voiry, I. Iatsunskyi, E. Coy, L. Mikoliunaite, S. Tumenas, K. Zaleski, Z. Balevicius, I. Baleviciute, A. Ramanavicius, S. Jurga, D. Erts, M. Bechelany. Tuning of structural and optical properties of Graphene/ZnO nanolaminates. *Journal of Physical Chemistry C* **2016**, *120*, 23716−23725, DOI: 10.1021/acs.jpcc.6b07221 *(impact factor = 4.536)*

8. **M. Baitimirova**, J. Andzane, G. Petersons, R. Meija, R. Poplausks, M. Romanova, D. Erts. Vapor-solid synthesis and enhanced thermoelectric properties of non-planar bismuth selenide nanoplates on graphene substrate. *Journal of Materials Science* **2016**, *51 (17)*, 8224-8232, DOI 10.1007/s10853-016-0097-z *(impact factor = 2.733)*

9. J. Kosmaca, J. Andzane, **M. Baitimirova**, F. Lombardi, D. Erts. Role of nanoelectromechanical swithching in the operation of nanostructured Bi_2Se_3 interlayers between conductive electrodes. *ACS Applied Materials & Interfaces* **2016**, *8 (19)*, 12257–12262, DOI: 10.1021/acsami.6b00406 *(impact factor = 7.78)*

10. J. Andzane, G. Kunakova, S. Charpentier, V. Hrkac, L. Kienle, **M. Baitimirova**, T. Bauch, F. Lombardi, D. Erts. Catalyst-free vapour-solid technique for deposition of Bi_2Te_3 and Bi_2Se_3 nanowires/nanobelts with topological insulator properties. *Nanoscale* **2015**, *7*, 15935–15944, DOI: 10.1039/c5nr04574f *(impact factor = 7.76)*

Papers not included in the thesis

11. D. Kulmatova, **M. Baitimirova**, U. Malinovskis, C.F. Chang, Y. Gu, A. Tamuleviciene, D. Erts, J. Prikulis. Photoluminescence and micro-extinction spectroscopy from zinc oxide nanorods with plasmonic nanoparticles. *Lithuanian Journal of Physics **2021**, 61,* 161-168 *(impact factor = 0.70)*

12. J. Maniks, V. Mitin, U. Kanders, V. Kovalenko, P. Nazarov, **M. Baitimirova**, R. Meija, R. Zabels, K. Kundzins, D. Erts. Deformation behavior and interfacial sliding in carbon/copper nanocomposite films deposited by high power DC magnetron sputtering. *Surface & Coatings Technology* **2015,** *276*, 279-285, doi: 10.1016/j.surfcoat.2015.07.004 *(impact factor = 2.53)*

13. **M. Baitimirova**, A. Pastare, J. Katkevics, A. Viksna, J. Prikulis, D. Erts. Gold nanowire synthesis by semi-immersed nanoporous anodic aluminum oxide templates in potassium dicyanoaurate-hexacyanoferrate electrolyte. *Micro & Nano Letters* **2014**, *9*, 761-765, doi: 10.1049/mnl.2014.0489 *(impact factor = 0.952)*

Author's contribution to publications:

1. Performed the synthesis of quartz/Bi_2Se_3/ZnO and graphene/Bi_2Se_3/ZnO nanostructures, performed EDX, XRD, absorption and photoluminescence spectra data analysis, was one of the main contributors to the manuscript writing.

2. Performed XRD data analysis of Bi_2Se_3 nanoribbons, contributed to manuscript writing.

3. Performed the experiments with the deposition of Bi_2Se_3 nanostructures on CVD graphene and mica, contributed to the manuscript writing.

4. Performed the synthesis of Bi_2Se_3 nanostructures onto graphene substrate, XRD data analysis, contributed to the manuscript writing.

5. Performed the synthesis of Bi_2Se_3 nanostructures onto graphene and quartz substrates, took part in the XRD and thermoelectric measurements data analysis, contributed to the manuscript writing.

6. Performed the synthesis of nanolaminates, took part in the XRD and Raman data analysis, contributed to the manuscript writing.

7. Performed the synthesis of nanolaminates and XRD, AFM, Raman data analysis, was one of the main contributors to the manuscript writing, prepared the manuscript for submission.

8. Performed experiments of Bi_2Se_3 nanostructures synthesis onto graphene, took part in analysis of SEM, TEM, AFM data, took part in thermoelectric properties measurements and analysis, contributed to the manuscript writing, prepared the manuscript for submission.

9. Performed synthesis of the Bi_2Se_3 nanostructures onto indium-tin-oxide, took part in carrying out the experiments on nanoelectromechanical switching of individual nanobelts, contributed to the manuscript writing.

10. Performed synthesis of Bi_2Se_3 nanowires/nanoribbons onto glass substrates, contributed to the manuscript writing.

International scientific conferences - a total of 23 reports, among them the most important are:

1. **M. Baitimirova**, J. Andzane, R. Viter, M. Bechelany, D. Erts. Graphene/Bi_2Se_3/ZnO heterostructures with enhanced photoluminescence of ZnO nanolayers. 12th International conference "Nanomaterials: Applications & Properties, IEEE NAP-2022", 11-16 September 2022, Krakow, Poland
2. **M. Baitimirova**, J. Andzane, R. Viter, B. Fraisse, O. Graniel, M. Bechelany, D. Peckus, S. Tamulevicius, D. Erts. Structure and optical properties of Bi_2Se_3/ZnO and graphene/Bi_2Se_3/ZnO heterostructures. International Conference "Nanomaterials for biosensors and biomedical applications", 2-4 July 2019, Jurmala, Latvia
3. **M. Baitimirova**, R. Viter, J. Andzane, I. Iatsunskyi, A. Ramanavicius, M. Bechelany, D. Erts. Nanolamination of graphene and ZnO in heterostructures. International conference "European Conference on Applications of Surface and Interface Analysis, ECASIA'17", 24-29 September, 2017, Montpellier, France
4. **M. Baitimirova**, J. Andzane, R. Poplausks, M. Romanova, D. Erts. Graphene/Bismuth selenide heterostructures for thermoelectric applications. International conference "Trends in Nanotechnology, TNT-2017", 5-9 June, 2017, Dresden, Germany
5. **M. Baitimirova**, R. Viter, J. Andzane, I. Iatsunskyi, V. Fedorenko, A. Ramanavicius, M. Bechelany, D. Erts. Influence of graphene on crystal structure of ZnO layers in Graphene/ZnO nanolaminates. 18th International conference "Advanced Materials and Technologies". 27-31 August, 2016, Palanga, Lithuania
6. **M. Baitimirova**, R. Viter, J. Andzane, D. Erts, M. Bechelany. Fabrication and characterization of ZnO/Graphene layered structures. International Conference „EuroNanoForum-2015", 10-12 June, 2015, Riga, Latvia
7. **M. Baitimirova**, D. Jevdokimovs, D. Erts, J. Andzane. Fabrication and properties of graphene/bismuth chalcogenide layered structures. 12th Russia/CIS/Baltic/Japan Symposium on Ferroelectricity and 9th International Conference Functional Materials and Nanotechnologies „RCBJSF-2014-FM&NT", 29 September – 2 October, 2014, Riga, Latvia

Annual international conferences of the University of Latvia and of the Institute of Solid State Physics: 12 and 4 papers, respectively.

1. LITERATURE OVERVIEW

1.1. Graphene, nanostructured bismuth selenide and zinc oxide, their mutual interaction in heterostructures

Due to the hexagonal structure of graphene, it is possible to grow nanostructures on its surface by van der Waals epitaxy, if the crystal lattices of the two materials match well (the crystal lattice mismatch should be <25% [12]).

Table 1.1. **Parameters of crystal lattices and their mutual compatibility [4, 9, 12]**

	Graphene	***Bismuth Selenide***	***Zinc Oxide***
Crystal system	hexagonal	rhombohedral	hexagonal
a = b, Å	2,46	4,14	3,25
c, Å	-	28,64	5,21
α (°)	-	90	90
β (°)	-	90	90
γ (°)	120	120	120
The distance between two atoms, Å	1,42	-	3,25
Schematic representation	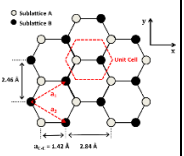	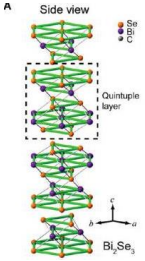	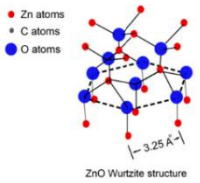
Compatibility with the graphene crystal lattice	-	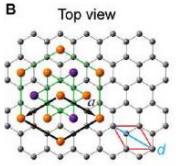	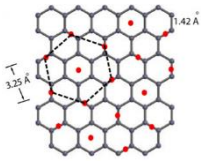
Lattice mismatch with the graphene crystal lattice, %	-	~2,9 %	~5 %

Bismuth selenide (Bi_2Se_3) is best suited for the synthesis of its nanostructures onto graphene. Bi_2Se_3 is known as one of the effective TE materials, and is sensitive to IR radiation. It is a topological insulator (a material that has the insulator properties in the volume, but is electroconductive on its surface) with the 0.3 eV band gap. The crystal lattice mismatch between the Bi_2Se_3 and graphene is about 2.9% [4] (Table 1.1). Typically, Bi_2Se_3 nanostructures grow by the Vollmer-Weber or island [13] growth model: the islands grow from the randomly arranged nucleation centers on the substrate and then coalesce to the continuous nanostructured layer. Factors such as substrate material, substrate temperature, flow of depositing material, etc. can affect the epitaxial growth. In the synthesis of Bi_2Se_3 nanostructures on the exfoliated multilayer graphene by the deposition method, the epitaxial growth is expressed in the formation of nanoplates oriented horizontally relative to the graphene surface, which is due to the above-mentioned small mismatch between graphene and Bi_2Se_3 [4].

Another semiconductor with a small (~5% [9], Table 1.1) crystal lattice mismatch with the graphene crystal lattice is zinc oxide (ZnO). ZnO is known as a semiconductor with a wide band gap (3.3 eV) and high exciton binding energy (60 meV) [14]. As a result, it exhibits pronounced luminescence already at room temperature. When graphene is used as a substrate for the hydrothermal synthesis of ZnO nanostructures, it promoted the arrangement of ZnO nanostructures in the nanowire array, and also improved the UV and Vis PL and photoconductivity of ZnO [9, 15]. There are demonstrations [16] where graphene has been successfully applied as a transparent top electrode in UV photodetectors based on ZnO nanowire arrays. However, no research has previously been reported where graphene-ZnO nanolaminates were fabricated, and the influence of graphene on ZnO properties (crystal growth, PL) and vice versa – the influence of ZnO layers on graphene properties (strain, charging) in these structures were studied.

The mechanism of improving the photosensitivity of ZnO by combining it with graphene is based on the charge transfer at the graphene-ZnO interface and on the decrease of the surface potential in the ZnO upper layers [16]. By this mechanism ZnO PL enhancement was demonstrated by combining ZnO with aluminum oxide (Al_2O_3, wide band gap or ~6 eV) in Al_2O_3/ZnO multilayer heterostructures or nanolaminates [17]. Fabrication of heterostructures from ZnO and narrow band gap materials (such as Bi_2Se_3, Bi_2Te_3) is advantageous for optoelectronic applications related to the photoactive charge separation in visible and NIR ranges. Recent theoretical studies [5] showed the possibility to enhance ZnO UV emission by surface plasmon (SPs) resonance. Due to the coupling between spin of the topological insulator and charge excitations of ZnO resulting from the locking of the spin and momentum, the PL increase is predicted. This is consistent with the research [18] that experimentally showed the ZnO PL enhancement by the placement of mechanically exfoliated Bi_2Te_3 flakes with a thickness below 200 nm on the surface of ZnO.

1.2. Synthesis of nanostructures by deposition methods

Graphene synthesis by *chemical vapor deposition (CVD)* with its subsequent transfer to the other surfaces is based on the splitting of hydrocarbon gas (most often – methane, less often – acetylene, hexane) into hydrogen and pure carbon at high temperature in the presence of a transition metal [19]. Copper foil is mostly used as a substrate and a catalyst for monolayer graphene synthesis. When the carbon-metal solid solution cools down during the synthesis process, carbon precipitates on the surface of the catalyst, forming a graphene structure.

After the synthesis, graphene is bonded to a copper substrate. To separate it from the substrate, a transfer procedure is performed. First, the graphene is coated with a polymer layer (most often - poly(methyl methacrylate) or PMMA), that acts as a support for the graphene coating when the copper substrate is etched. At the initial stages of copper etching, diluted nitric acid is used because of the high oxidation-reduction reaction rate. This makes possible to dissolve a thicker layer of copper quickly. However, nitric acid is not used for the complete etching of the copper substrate as the nitrogen monoxide gas bubbles, formed as a result of the reaction, can crack the graphene layer. For the further etching, less aggressive reagent such as iron (III) chloride is used. It dissolves copper effectively, without forming gaseous and solid reaction products [20]. After etching the substrate, the graphene/PMMA samples are transferred to the target substrate and dried. Then the PMMA layer is removed by dissolving it in acetone and burning its residues at 400 °C in a mixture of argon and hydrogen gases [21].

Physical vapor deposition (PVD) is one of the simplest methods for the synthesis of nanostructures. It is based on the evaporation of a solid source material at high temperature under low-pressure conditions, and its desublimation in a from of nanostructures on a substrate located in a certain lower temperature region. For Bi_2Se_3 nanostructures synthesis, 99.999% Bi_2Se_3 powder or crystals are used as a source material. The synthesis process requires a constant flow of inert gas to transfer the vapors of the source material from the evaporation region to the deposition region where the substrate is placed. Upon reaching the substrate with lower temperature, supersaturated vapor is formed, resulting in material deposition on the substrate, nucleation and growth of the nanostructures.

Due to the optical transmission, low thermal conductivity, and non-conductive properties quartz is commonly used as a substrate for PVD synthesis for optical, electrical, and thermoelectric measurements. Quartz can be replaced by a glass as a cheaper alternative with the similar properties. Nanostructures can also be synthesized on mica and silicon substrates. During the synthesis process, using a constant inert gas flow, a mixture of nanostructures consisting of nanowires, nanoribbons and individual nanoplates is deposited on such substrates [22]. Gold or titanium oxide nanoparticles [23, 24] can be used for the synthesis of Bi_2Se_3 nanoribbons/nanowires, where they act as nucleation centers

for the growth of Bi_2Se_3 nanostructures. However, such structures will contain impurities introduced by the used catalysts.

The atomic layer deposition (ALD) method is based on sequential, self-limiting reactions from the gas phase, that take place in a controlled manner on the substrate surface. Using this method, nanostructures grow layer-by-layer by sequential deposition of atomic layers. This allows to control growth mechanism at the nanoscale and obtain high-quality uniform thin films with precise thickness, that perfectly cover the surface of the substrate of any morphology [25].

Figure 1.1. **Deposition mechanism of ZnO nanostructures using atomic layer deposition method [26]**

In the ALD synthesis of ZnO nanostructures, the substrate is sequentially treated with diethylzinc $Zn(C_2H_5)_2$ and water vapor (Figure 1.1), removing the reagent residues with an inert gas before the injection of the next reagent. An oxide surface, that typically covered with hydroxyl groups, is commonly used as a starting surface for the ALD synthesis process (e.g., Si/SiO_2). The step 1 of ALD is the exposure of the substrate to diethylzinc $Zn(CH_2CH_3)_2$ precursor molecules that adsorb at the surface in a reaction with the OH-groups. As a result of chemisorption, O-Zn bonds are formed and ethane C_2H_6 is released as reaction product. Ideally, after step 1, all OH-groups on the surface of the substrate have reacted and contain a - (CH_2CH_3) group. After the excess diethylzinc molecules have been removed (step 2), water is introduced as the second reactant of the synthesis reaction (step 3). The -(CH_2CH_3) groups adsorbed on the surface react with the H_2O molecules. This results in the formation of new -OH groups on the substrate surface and C_2H_6 molecules are released as reaction product. After the purge of the H_2O excess and reaction byproducts, the ALD cycle is repeated until the ZnO layer of the desired thickness has grown [26]. Typically, the one ALD cycle results in the deposition of ZnO monolayer with the thickness of 2.5 Å [27].

2. EXPERIMENTAL SECTION

2.1. Synthesis of nanostructures

For the fabrication of nanostructures, graphene was synthesized on the electrochemically polished copper substrate (GoodFellow, 99.9%) using the CVD reactor First Nano Easy tube 101 (UL Institute of Chemical Physics, Latvia). Then graphene monolayers were transferred onto quartz substrates or nanostructures by polymer-assisted transfer technique [21, 28-29].

Bi_2Se_3 nanostructures were synthesized on non-conductive (quartz, glass, AAO) and conductive (graphene, ITO) substrates using PVD method. Bi_2Se_3 source material (99.999%, "Sigma-Aldrich") was heated in a high-temperature vacuum furnace GSL-1100X, MTI Corp (UL Institute of Chemical Physics, Latvia) for 15 min at 585 °C temperature, under low-pressure conditions, with the initial pressure of 200 mTorr. Due to the high temperature, the Bi_2Se_3 source material evaporated and deposited on substrates placed downstream in the 330-380 °C temperature region of the quartz tube (see temperature distribution on the substrate during the synthesis in Figure 2.1). When the furnace was naturally cooled down to 535 °C, the N_2 carrier gas flow (35 Torr) was introduced into the furnace tube during the cooling process in the temperature interval 535-470 °C. After that, the furnace tube was filled with N_2 up to atmospheric pressure, sealed and cooled down to room temperature. For the comparison Bi_2Se_3 nanostructures were synthesized by the same method, but without N_2 gas flow (the synthesis process occurs inside the evacuated and sealed quartz tube in absence of gas flow).

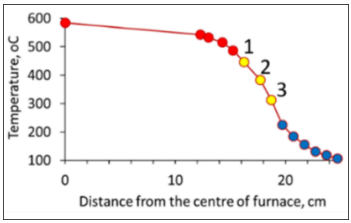

Figure 2.1. **Temperature distribution in the quartz tube furnace (yellow dots correspond to the temperature on the substrate): 1) 445 °C, 2) 380 °C, 3) 310 °C**

For the fabrication of G/ZnO nanolaminates and Bi_2Se_3/ZnO heterostructures, ZnO nanolayers of different thicknesses (from 10 to 100 nm) were synthesized on prepared graphene and on the Bi_2Se_3 nanostructures by the atomic layer deposition method using a home-made ALD reactor (European Institute of Membranes, University of Montpellier, France) under the same conditions as previously synthesized and studied ALD ZnO thin films [27]. For the comparison, ZnO layers were also synthesized on p-doped Si substrates

((100), Sir-Mat). Diethylzinc (95%, STREM Chemicals Inc.) was used as zinc precursor and water was used as an oxidant. The ZnO growth rate was 0.2 nm/cycle at 100 °C temperature.

2.2. Characterization methods of nanostructures

The morphology and chemical composition of the synthesized nanostructures were evaluated using a scanning electron microscope (SEM) Hitachi S4800 equipped with energy dispersive X-ray (EDX) analyser Bruker Nano XFlash 5010 (UL Institute of Chemical Physics, Latvia).

To determine the crystalline structure and the thickness of the nanolayers, as well as to evaluate the interdiffusion of materials in layered structures, the samples were studied using high-resolution transmission electron microscopes - Fei Tecnai CF20 (200 kV), equipped with EDX detector EDAX (UL Institute of Solid State Physics, Latvia), Jeol ARM 200F (200 kV) (NanoBioMedical Center, Poland) and Fei Titan (300 kV) equipped with EDX detector EDAX (Los Alamos National Laboratory, USA). Individual nanostructures were mechanically transferred onto a TEM grid. The electron-transparent cross-section lamellas were prepared by focused ion beam (FIB) Jeol JIB-4000 (NanoBioMedical Center, Poland) or Thermo Fisher Scientific Scios 2 Dual Beam SEM/FIB (Los Alamos National Laboratory, USA) milling and lift-out. The FIB lamellas were attached to a Cu half grid and further thinned by low keV milling using the Ga^+ beam.

The crystalline structure of the synthesized nanostructures was studied using powder X-ray diffractometer Bruker D5000 with Cu Kα radiation and PANalytical X'Pert MRD with Cu Kα radiation using the grazing incidence mode (both at the European Membrane Institute, France).

The surface morphology of the Bi_2Se_3 nanostructured coatings was characterised by atomic force microscope (AFM) Asylum Research MFP-3D (UL Institute of Chemical Physics, Latvia) using Olympus AC160TS AFM tips. Because of the limitations of the AFM tip shape [30], the slope angles of the nanostructures were possible to determine with maxima up to 65° relative to the surface of the substrate.

2.3. Methods of characterizing electroconductive, thermoelectric and optical properties of layered nanostructures

Electrical characterisation of the nanostructured coatings was carried out using a Keithley 6430 picoammeter/voltage source (UL Institute of Chemical Physics).

Thermoelectric measurements were performed at room temperature using a Peltier elements-based measuring device calibrated for the temperature range

295-320 K by the Standard Reference Material 3451 (NIST) for low-temperature Seebeck coefficient (10-390K) (UL Institute of Chemical Physics). For determination of the thermoelectric response of the nanostructured coatings to IR illumination, 3 min long impulses by an IR diode (940 nm, 0.1 W/cm^2, irradiation spot diameter 6 mm) were used). HP34401A voltmeter connected to a computer with laboratory-developed software was used for recording both thermally induced voltage.

Optical properties of fabricated layered structures were determined by Raman spectroscopy using a Witek ALFA300R Raman spectrometer with a 532 nm excitation laser source (State Research Institute Center for Physical Sciences and Technology, Lithuania). UV-Vis reflectance/transmittance spectra were obtained by UV-Vis reflectance spectrometer Shimadzu UV-3600 (State Research Institute Center for Physical Sciences and Technology, Lithuania) and optical fiber spectrometer Ocean Optics HR2000+ (UL Institute of Atomic Physics and Spectroscopy, Latvia). PL spectra were analyzed in the wavelength range 340-775 nm using Edinburg Instruments FLS 980 PL measurement spectrometer with a Xe lamp line, centered at 280 nm wavelength (State Research Institute Center for Physical Sciences and Technology, Lithuania) and Ocean Optics HR2000+ fiber optic spectrometer with nitrogen lasers with 266 nm excitation wavelength (UL Institute of Atomic Physics and Spectroscopy, Latvia). The obtained PL spectra were deconvoluted using MagicPlot 2.7.1.0 software by splitting the spectra in separate peaks with the Gaussian fitting, keeping maxima positions of all subpeaks fixed within ±0.02 eV and full width at half-maximum within ±0.03 eV.

3. RESULTS AND DISCUSSION

3.1. Graphene/Bi_2Se_3 layered nanostructures for applications in thermoelectric devices

3.1.1. Synthesis and morphology of Bi_2Se_3 nanostructures on different substrates

The results of this chapter are described in the publications № 2, 4, 9 and 10.

As the type of the substrate used for the nanostructure synthesis by physical vapour deposition method can influence the morphology and properties of the deposited nanostructures, it is important to study the growth mechanisms of Bi_2Se_3 nanostructures on different substrates before the synthesis of layered nanostructures.

Figure 3.1 shows the SEM images of Bi_2Se_3 nanostructures obtained by the catalyst-free PVD method on different substrates (glass, quartz ITO, AAO). Bi_2Se_3 nanoplates oriented at different angles relative to the surface of the substrate were obtained (150-200 nm thick, 0.5-2.5 μm wide) on glass and non-passivated fused quartz substrates. These nanoplates coalesce and form a continuous nanostructured coating (Figure 3.1.a, b). Such substrates have unsaturated (dangling) bonds originating from the surface defects of quartz. These dangling bonds introduce defects in the crystalline structure of growing nanoplates and promote the formation of nanoplates oriented in different directions.

The carrier gas flow introduced at the certain temperature interval during the cooling stage of the synthesis process results in an increase of the Bi_2Se_3 concentration delivered to the substrate, thus breaking the symmetry of the nanoplates and promoting growth only in one specific direction. This results in the formation of up to 50 μm long nanoribbons (average density is approx. 2 pcs/1000 μm^2). Initially formed during the synthesis process nanoplates serve as the nucleation centers of nanoribbons (Figure 3.1.c, inset).

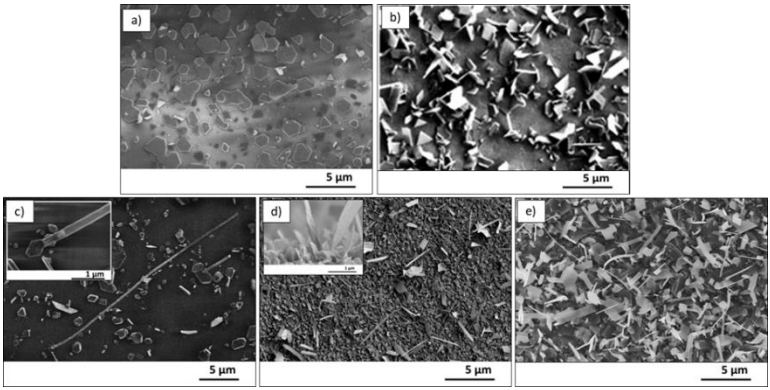

Figure 3.1. **SEM images of nanostructured Bi_2Se_3 on different substrates: nanoplates on quartz/glass (a), a nanostructured coating consisting of the coalesced nanoplates oriented at different angles relative to the quartz/glass substrate (b), nanoribbons obtained on quartz (c), indium tin oxide (d) and anodized aluminum oxide substrates (e)**

Similarly to the growth on quartz/glass substrates, the use of carrier gas flow during the certain temperature range of the cooling stage of the synthesis process promotes the growth of the nanoribbons and individual nanoplates oriented at different angles relative to the ITO glass substrate (Figure 3.1.d). In case of the ITO substrate, the tin acts as catalyst for the growth of Bi_2Se_3 nanostructures, similarly to the growth of Bi_2Se_3 nanoribbons by PVD using titanium oxide nanoparticles [24] and gold nanoparticles [31] as catalysts or ZnTe nanowires on fluorine-doped tin oxide (FTO) substrates [32]. Due to the presence of catalyst (ITO substrate), the average density of Bi_2Se_3 nanoribbons increased approx. 2 times in comparison with the catalyst-free synthesis on glass/quartz substrates, i.e. average density of nanoribbons was approx. 5 pcs/1000 μm^2.

In comparison with glass/quartz and ITO substrates, the AAO substrate is more suitable for the catalyst-free synthesis of Bi_2Se_3 nanoribbons (Figure 3.1.e). The average density of the nanoribbons obtained on it was 20 pcs/1000 μm^2, that is approx. 10 and 4 times more than it was obtained on glass/quartz and ITO substrates, respectively. The ordered porous AAO surface with high surface roughness/irregularities and funnel-type pore openings promotes the formation of oriented under different angles relative to the substrate surface nanoplates, that serve as nucleation centers of nanoribbons. The growth of Bi_2Se_3 nanoribbons occurs by the same mechanisms such as on glass/quartz substrates, i.e. the growth starts from non-hexagonal shape nanoplates or from the disordered nanoplate stackings.

3.1.2. Synthesis of Bi_2Se_3 nanostructures on graphene

The results of this chapter are described in the publications № 3, 4 and 8.

SEM images of the individual Bi_2Se_3 nanostructures and nanostructured coatings synthesized on graphene are shown in Figure 3.2. Due to the small crystal lattice mismatch of graphene and Bi_2Se_3 as well as due to the fact that the graphene substrate has no dangling bonds on its surface, the Bi_2Se_3 nanostructures grow epitaxially on the graphene substrates. Horizontally oriented nanoplates (0.5-3 μm wide) coalesce together, forming 150-300 nm thick continuous nanostructured coatings (Figure 3.2.a,b). Such nanostructured coatings cannot be obtained on not-passivated fused quartz of glass substrates due to the influence of chemical surface defects originating from their structure [33].

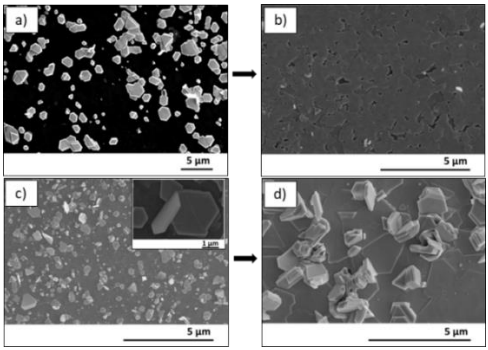

Figure 3.2. **SEM images of Bi_2Se_3 nanostructures grown onto graphene substrates: individual horizontally oriented nanoplates (a), that coalesce into nanostructured coating (b), individual nanoplates oriented under different angles relative to the substrate surface (c), that coalesce into nanostructured coating (d)**

The use of carrier gas flow at the certain temperature interval during the cooling stage of the synthesis process causes a rapid increase of the concentration of vaporized source material in the deposition area, thereby hampering the horizontal growth of nanoplates and promoting the formation of the nanoplates oriented under different angles at the facing edges of the grain boundaries of horizontally oriented nanoplates (Figure 3.2.c). This results in formation of continuous 100-200 nm thick nanostructured coatings consisting from coalesced nanoplates oriented under different angles relative to the substrate surface (Figure 3.2.d). The density of the obtained onto graphene individual Bi_2Se_3 nanoplates oriented at different angles relative to the substrate surface was approx. $15 \cdot 10^4$ pcs/ mm^2, and in the nanostructured coating was about $(25 - 40) \cdot 10^4$ pcs/ mm^2.

In contradiction to the glass/quartz substrates, the graphene substrate has high thermal conductivity. Thus, while temporary gas flow causes temperature gradient across the previously formed horizontally oriented nanoplates formed on a glass/quartz substrate, thus breaking the nanoplate growth symmetry and promoting one-direction growth of nanoribbons, the graphene substrate equalises the temperatures across the horizontally oriented nanoplates, preventing further one-direction growth of the nanoplate and formation of the nanobelt-like structures.

The Bi:Se atomic mass percentage of non-planar Bi_2Se_3 nanoplates, calculated from the intensities of K_M and K_L lines in the EDX spectrum, was 40:60 at%, respectively, confirming the stoichiometric Bi_2Se_3 compound.

High-resolution TEM images of Bi_2Se_3 nanoplates obtained on graphene substrates (Figure 3.3) show that the nanoplates are single-crystalline and their surface is covered with an amorphous native oxide layer, which is the result of Bi_2Se_3 oxidation under ambient conditions [34]. The single-crystalline structure of Bi_2Se_3 nanoplates was confirmed by the perfectly symmetrical hexagonal spot pattern obtained in the fast Fourier transform (FFT) image (Figure 3.3.b, inset) and in the selected area electron diffraction (SAED) pattern (Figure 3.3.c).

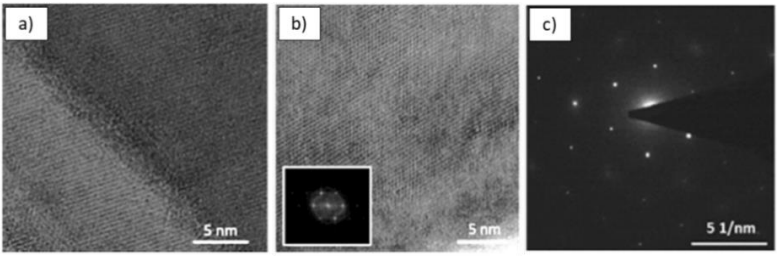

Figure 3.3. **High-resolution TEM images of Bi_2Se_3 nanoplates synthesized on graphene: a nanoplate edge highlighting the layered structure of the nanoplate with formed terraces (a), the single-crystalline structure of the nanoplate and corresponding FFT image (b) and SAED pattern of the nanoplate (c)**

The calculated from SAED and FFT images lattice spacing between the atom stacks in the nanoplate grown on from the graphene substrate was 3.5 ± 0.1 Å, that corresponds to the (101) crystallographic plane of stoichiometric Bi_2Se_3 with rhombohedral crystal structure with the unit cell lattice constants $\alpha \sim 4.140$ Å and $c \sim 28.636$ Å [35, 36].

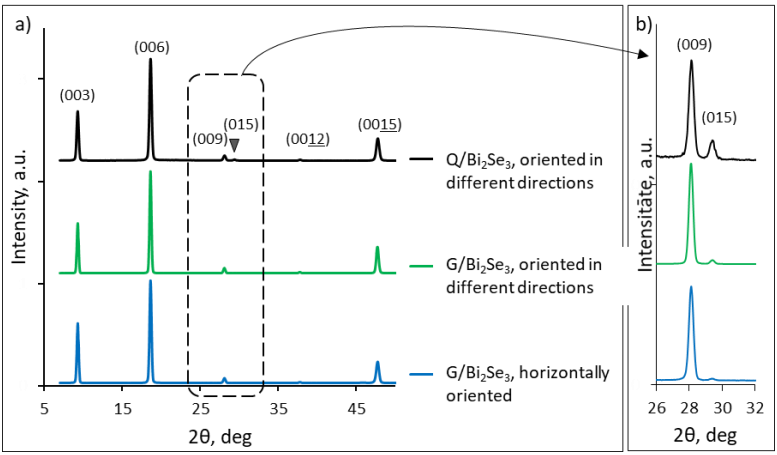

Figure 3.4. **XRD patterns of Bi_2Se_3 nanostructured coatings consisting from coalesced nanoplates oriented under different angles relative to the surface of graphene (G) and quartz (Q) substrates: a) full range of spectra, b) magnification of spectra**

In turn, the observed diffraction peaks at the XRD patterns of Bi_2Se_3 nanostructured coatings of different morphology (coalesced horizontally oriented nanoplates onto graphene and coalesced nanoplates oriented under different angles onto graphene and quartz substrates) indicate that the growth of Bi_2Se_3 nanostructures mainly is in the [00*l*] direction, which means parallel to the surface of the substrate (Figure 3.4). Closer look at the XRD patterns shows that the intensity of (015) diffraction peak (2θ position is 29.38° [35]) for Bi_2Se_3 coating consisting of coalesced horizontally oriented nanoplates onto graphene substrate is negligible, while 23lightly raises for the coatings of nanoplates oriented under different angles on a graphene substrate, and becomes well-noticeable for the Bi_2Se_3 coating formed by the nanoplates oriented under different angles and grown on a quartz substrate (Figure 3.4.b). This corresponds to the SEM images of the nanostructured coatings, showing a higher proportion of the oriented under different angles relative to the substrate surface nanoplates per unit area for the nanostructured coating deposited on a quartz substrate in comparison with the coating deposited on a graphene substrate (Figure 3.1.b and 3.2.b, d).

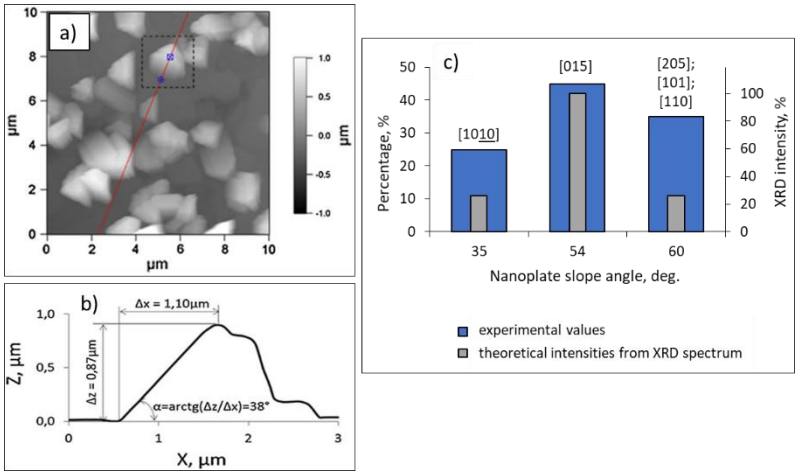

Figure 3.5. **(a) an AFM image of a Bi_2Se_3 nanostructured coating consisting from coalesced oriented under different angles nanoplates grown on graphene substrate; (b) an example of height profile and orientation angle calculation; (c) slope angle histogram of the oriented under different angles relative to the substrate surface nanoplates (Labels shows presumable growth direction of the nanoplates, assumed from the X-ray diffractogram)**

The slope angles or orientation angles of the randomly oriented relative to the graphene substrate surface individual nanoplates were determined from the AFM images (Figure 3.5.a, b) and were compared with the orientation angles of main crystallographic planes of the stoichiometric Bi_2Se_3, calculated relative to the (001) crystallographic plane. Taking the measurement accuracy of ±5°, as the coalesced horizontally oriented nanoplates might be not strictly parallel to the graphene substrate surface (e.g., may be oriented at an angle of approx. 5-15°), and assuming that the growth of non-horizontally oriented nanoplatelets occurs along the main crystallographic directions characteristic for the Bi_2Se_3, the orientation angle distribution of non-horizontal nanoplates is the following (Figure 3.5.c): 45% of the nanoplates grow under orientation angle of 54°±5° relative to the graphene surface, which can be attributed to [015] growth direction, while 30% of the nanoplates are oriented under angles >65°. Within the AFM measurement accuracy, the growth directions of the nanoplates oriented under an angle >65° can be attributed to any of ([205], [101] and [110] crystallographic growth directions (orientation angles 70°, 82° and 90°, respectively), that cannot be identified precisely using this method. The remaining 25% of the non-horizontal nanoplates have an orientation angle of 35°± 5° and may correspond to [10$\underline{1}$0] crystallographic growth direction. Determined from the AFM images [101] and [015] crystallographic growth

directions of Bi_2Se_3 nanoplates are in agreement with the directions determined from the SAED and XRD data.

3.1.3. Electrical and thermoelectric properties of graphene/Bi_2Se_3 layered nanostructures

The results of this chapter are described in the publications № 5 and 8.

For characterisation of G/Bi_2Se_3 nanostructured coatings, the sandwich-like G/Bi_2Se_3/G structures were fabricated by the mechanical placing of pre-transferred on a quartz substrate graphene monolayer on top of Bi_2Se_3 nanostructured coating, grown on another quartz/graphene substrate (Figure 3.6). Thus, the Bi_2Se_3 nanostructures were located between the graphene monolayers serving as electrodes. The electrical and thermoelectric properties of these layered structures were determined by *through-plane* measurements.

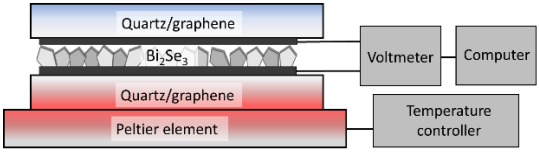

Figure 3.6. **Schematic representation of the experimental setup for the investigation of electrical and thermoelectric properties of graphene/Bi_2Se_3/graphene layered structures**

The current-voltage (*I*-*V*) curves of the fabricated layered G/Bi_2Se_3/G structures are linear (Figure 3.7.a), indicating well-formed ohmic contacts between the graphene layers and Bi_2Se_3 nanostructured coatings despite the fact that one contact with graphene was made mechanically. At the same time, the electrical conductance of the nanoplates oriented under different angles is lower in comparison with the conductance of the horizontally oriented nanoplates. This can be explained by the fact that in the mechanically established contacts the electrical connections made with the graphene layer by non-horizontally oriented nanoplates are dominating. As a result, the electrical contact area is lower in comparison with the contact between the graphene layer and horizontally oriented nanoplates.

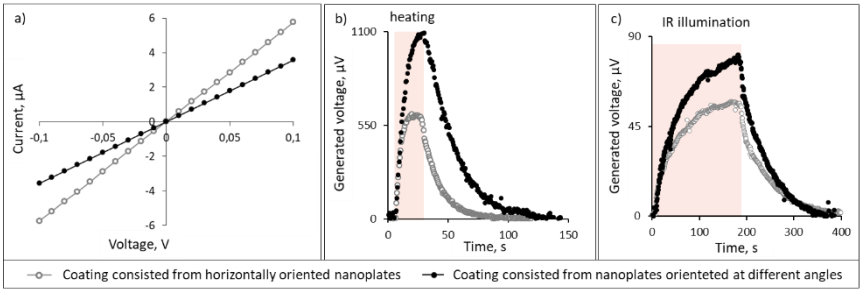

Figure 3.7. **(a) Current-voltage characteristics, (b) thermoelectric voltage induced due to applied temperature gradient and (c) infrared illumination of graphene/Bi_2Se_3/graphene layered structures based on horizontally oriented nanoplates and nanoplates oriented under different angles relative to the substrate surface.**

The voltage generated by the G/Bi_2Se_3/G layered structures in response to the applied for about 20 s (illustrated in Figure 3.7.b as rectangle) between top and bottom graphene electrodes temperature gradient of 16 °C is nearly 2 times higher for nanoplates, oriented under different angles in comparison with horizontally oriented nanoplates (1100 μV vs 600 μV). Similarly to the thermoelectric response to direct thermal exposure, Bi_2Se_3 nanostructured coating consisted from the randomly oriented nanoplates showed about 1.5 times higher response to IR illumination in comparison with the Bi_2Se_3 nanostructured coating consisted from horizontally oriented nanoplates (Figure 3.7.c), i.e. 80 μV and 55 μV respectively. Thus, significant thermoelectric response and response to IR illumination, demonstrated by G/Bi_2Se_3/G layered structures based on the Bi_2Se_3 nanoplates oriented under different angles, proves the potential for application of these layered structures in thermoelectric devices and IR sensors.

3.2. Graphene/ZnO nanolaminates for sensor applications

3.2.1. Structure of graphene/ZnO nanolaminates

The results of this chapter are described in the publications № 6 and 7.

The fabricated G/ZnO nanolaminates with different thicknesses of ZnO interlayers (from 10 to 100 nm) were named by the formula $G_{x,L}ZnO_{y,nm}$, where *xL* is the number of graphene layers (*L*) and *y* is the thickness in nanometers of ZnO single layer in multilayer structure.

High-resolution cross-section TEM images confirmed the sequence of alternating ZnO and graphene layers throughout all fabricated G/ZnO nanolaminates (Figure 3.8). The total thickness of all obtained G/ZnO nanolaminates was about 100 nm. The individual ZnO layers were of constant thickness and well reproducible.

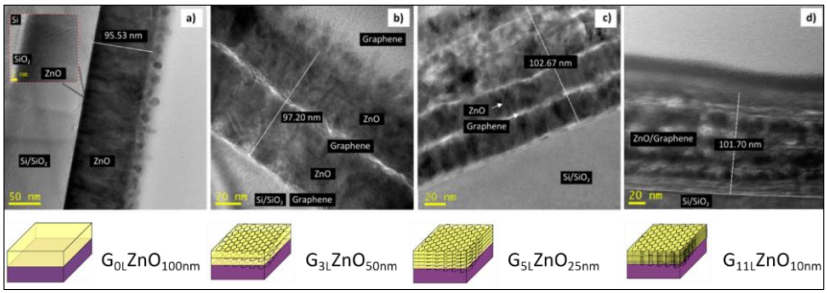

Figure 3.8. **High-resolution TEM images of cross-sections of the nanolaminates: a) ZnO layer on Si substrate or $G_{0L}ZnO_{100nm}$, b) $G_{3L}ZnO_{50nm}$, c) $G_{5L}ZnO_{25nm}$, d) $G_{11L}ZnO_{10nm}$**

The high-resolution TEM analysis of G/ZnO nanolaminates showed the presence of (100), (002), (101), (110) and (103) crystallographic planes in the selected area of the ZnO layer (Figure 3.9.a), indicating its polycrystallinity. Obtained XRD spectra of ZnO layers of G/ZnO nanolaminates showed similar data on crystallographic planes (Figure 3.9.b). Calculated from the XRD spectra ZnO lattice constants were equal to a = 0.325 nm and c = 0.519 nm, which fits perfectly with the ZnO crystal lattice parameters (a = 0.325 nm and c = 0.521 nm [37]).

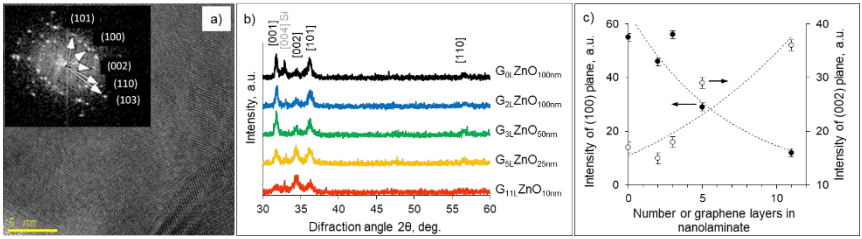

Figure 3.9. **High-resolution TEM image of ZnO interlayer of the sample $G_{11L}ZnO_{10nm}$ (a) and FFT image of this area (inset). X-ray diffraction patterns of ZnO thin film and graphene/ZnO nanolaminates (b) and curves illustrating intensities of diffraction peaks of (100) plane (primary y scale) and of (002) plane (secondary y scale) versus number of graphene layers in the G/ZnO nanolaminates (c)**

No amorphous-to-crystalline growth transition of ZnO was observed. As it can be seen from the XRD and TEM data obtained for the G/ZnO nanolaminates, even the 10 nm thick ZnO layers have a crystalline nature ($G_{11L}ZnO_{10nm}$ Figure 3.9.a, b).This contradicts with the previous reports on ZnO thin films [27] and Al_2O_3/ZnO nanolaminates [17], deposited by ALD on Si/ SiO_2 substrates. In these reports, the amorphous-to-crystalline transition of ZnO was reported to occur for the layers with thickness larger than 25 and 10 nm, respectively.

From the intensities of the diffraction peaks in XRD patterns of nanolaminates (Figure 3.9.a, b) it can be seen that for the 10 and 25 nm thick ZnO interlayers, the [002] crystal growth direction is dominating. Presumably, the graphene sublayers promote growth of ZnO crystalline transition layer in [002] direction. This can be attributed to the very small (<5% [9]) mismatch between the graphene and ZnO hexagonal lattices. These results suggest the advantageous role of graphene as a substrate in the cases where crystalline ZnO thin films are required.

To evaluate possible deformation (i.e. stress [38]) of graphene and charge transfer through the graphene-ZnO interface, Raman spectra of the fabricated G/ZnO nanolaminates were analysed (Figure 3.10.a). Characteristic for graphene G (1583 cm^{-1}) and 2D (2671 cm^{-1}) bands corresponding to the basis and secondary vibrations of sp^2-hybridized carbons, respectively [39], were observed in all spectra obtained. Both G and 2D peaks were sharp, indicating that no oxidation of graphene to graphene oxide [40] occurred during the formation of ALD ZnO layers. This suggests that the high quality of graphene is largely preserved after the formation of the multilayer structure.

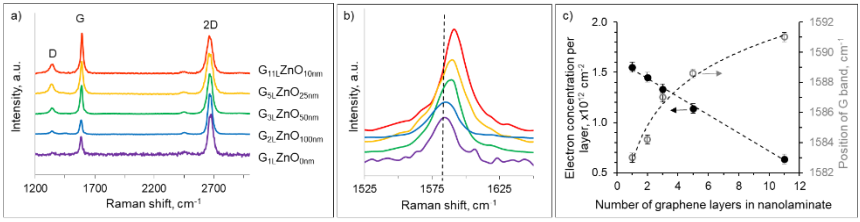

Figure 3.10. **Raman spectra of graphene and G/ZnO nanolaminates (a), close view of G band shifting (b), curves illustrating shifting of G band (secondary y scale) and charge per graphene monolayer (primary y scale) versus number of graphene layers in the G/ZnO nanolaminates (c)**

The ratio of intensities of the 2D band to the G band (I_{2D}/I_G) of single CVD graphene layers was above 2, confirming the monolayer structure of this graphene [41]. The detected low intensity of the D band at 1350 cm^{-1} in the spectra indicated the presence of insignificant amount of structural defects in the monolayer, which is typical for the CVD graphene [42]. When ZnO layers of different thicknesses were synthesized on graphene, the I_D/I_G ratio moderately increased from 0.1 for a single graphene monolayer to ~0.22 for the G/ZnO nanolaminates. Thereby, in contradiction with sputtering techniques (e.g. RF sputtering), where a significant increase in the I_D/I_G peak intensity ratio up to 1 [43] is typically observed after ZnO deposition on the graphene substrate, the ALD deposition of the ZnO on graphene surface does not induce severe structural damage in it.

The I_{2D}/I_G ratio in the Raman spectra of the G/ZnO nanolaminates decreased from 2.68 for the nanolaminate containing two graphene layers

$G_{2L}ZnO_{100nm}$ to 1.33 and 1.20 for $G_{3L}ZnO_{50nm}$ and $G_{5L}ZnO_{25nm}$ structures containing three and five graphene layers, respectively, and further down to 0.87 for the $G_{11L}ZnO_{10nm}$ nanolaminate containing 11 graphene layers. These changes in the I_{2D}/I_G intensity ratios may be related to such processes as charging [44] and/or mechanically induced strain [38], occurring in the graphene layers of nanolaminates. However, the typical for uniaxial of biaxial graphene strain redshifts of either G or 2D peaks by 30-50 cm^{-1} per 0.5% of strain [38] were not observed in the obtained Raman spectra. The position of the 2D band remained unchanged and the position of the G band shifted in opposite direction, i.e. blueshifted (Figure 3.10.a, b). This suggests that the graphene interlayers in G/ZnO nanolaminates do not experience significant strain and the changes in the positions and intensity ratios of G and 2D peaks are mostly related to the graphene charging, which is related to the charge carriers transfer through the graphene-ZnO interface and supports by the observed blue-shift of G band position. G band position blue-shifted with the increase of the number of graphene interlayers and respectively decrease of thickness of ZnO interlayers (Figure 3.10.b). The above changes in Raman spectra of G/ZnO nanolaminates may be attributed to the negative charge of graphene by the electron transfer from ZnO layers. Presumably, this electron transfer from ZnO to graphene results in the formation of the depletion layer in ZnO near the graphene surface, and facilitates accumulation of holes in it.

For quantifying the graphene charge in the G/ZnO nanolaminates, the estimation of concentration of excess electrons per graphene layer was performed on the basis of data reported on the interdependence between Raman shift of G band and the increase of concentration of electrons in monolayer graphene [44]. It was found that the negative charge per graphene layer linearly decreases with the increase of number of graphene layers and respectively with the decrease of thickness of ZnO interlayers (Figure 3.10.c). The decrease of the graphene charge may be related to the interaction and overlapping of ZnO depletion layers with the decrease of ZnO interlayer thickness, as well as to the change of defect concentration in ZnO interlayers, related to the change of prevailing crystallographic ZnO growth direction with the decrease of interlayer thickness. Such linear dependence of graphene charge on the number of graphene layers in G/ZnO nanolaminates may be useful in charge-related applications, for example, for tuning graphene charge by varying the number of graphene interlayers in the nanolaminates for selective adsorption of positively charged target molecules on the graphene surface.

3.2.2. Optical properties of graphene/ZnO nanolaminates

The results of this chapter are described in the publication № 7.

The number of graphene layers and thickness of ZnO interlayers in G/ZnO nanolaminates have strong influence on their optical properties. The shift of ZnO

absorption edges relative to the absorption edge position of pure ZnO (Figure 3.11.a) from 360 to 400 nm is clearly seen in the reflectance spectra recorded for different G/ZnO nanolaminates. This may be related to the formation of optically active defects in the graphene-ZnO nanolaminates and at the ZnO grain boundaries.

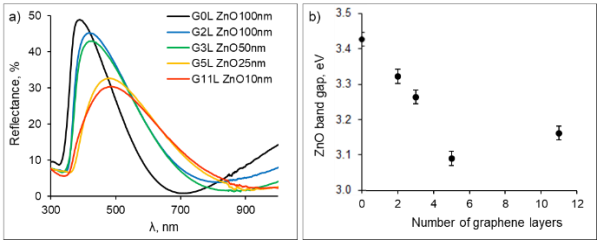

Figure 3.11. **Reflectance spectra (a) and dependence of the ZnO band gap on the number of graphene layers (b) of ZnO thin film and G/ZnO nanolaminates**

The determined from the reflectance spectra band gap values of ZnO decrease with the increase of the number of graphene layers and the decrease of thickness of ZnO layers in nanolaminates from the initial value of 3.42 eV, obtained for pure ZnO thin film, down to the value of 3.10–3.13 eV for the nanolaminates containing five and more for graphene layers, respectively (Figure 3.11.b). The leveling of the band gap at these values may be related to the domination of ZnO [002] crystallographic growth direction over other directions for the ZnO interlayer thickness below 25 nm as confirmed by XRD data (Figure 3.9.c). This may reduce the concentration of optically active defects.

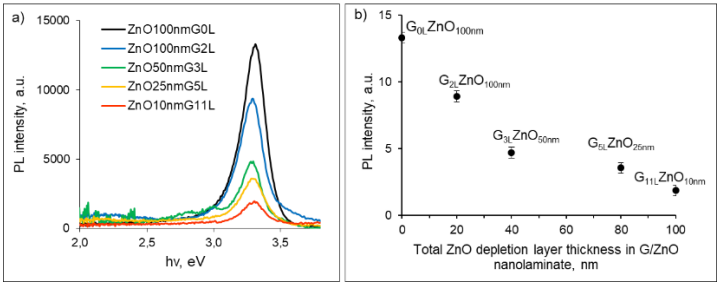

Figure 3.12. **Photoluminescence spectra of ZnO thin film and G/ZnO nanolaminates (a), photoluminescence intensity versus presumed summed thickness of ZnO layer affected by PL suppressive factors in G/ZnO nanolaminates (calculated assuming 10 nm thick ZnO affected by PL suppressive factors near every surface of individual graphene layers) (b)**

In the PL spectra of G/ZnO nanolaminates (Figure 3.12.a), related to exciton transitions in ZnO [27, 46] the peak with maximum at ~3.3 eV (375 nm)

was observed for all obtained samples. PL peaks at energies about 2.4-2.5 eV (oxygen and zinc vacancies, zinc interstitials [47], as well as at 2.0 eV (oxygen iterstitials in ZnO layers [47]) were not observed for both ZnO thin film deposited on Si and for G/ZnO nanolaminates. From Figure 3.12.a it is clearly seen that the intensity of PL signals decreased with the increase of number of graphene layers and the corresponding decrease of the thickness of ZnO interlayers in G/ZnO nanolaminates. PL emission may be quenched because of several reasons, such as negative charge of graphene surface, with concomitant screening effect in graphene [48], transfer and trapping of photoexcited electrons in graphene [10, 49], as well as increase of the total depletion reġions relative to total thickness of ZnO when decreasing the ZnO layer thickness [17]. These factors result in the decrease of exciton luminescence of G/ZnO nanolaminates with the increase of the number of graphene layers and decrease of thickness of ZnO layers.

The presumable thickness of the depleted ZnO layer with fully quenched PL near the single surface of a graphene layer was estimated by empirical linearization of PL luminescence intensity as function of summed all quenched ZnO layer thicknesses in the G/ZnO nanolaminates. The closest to a linear curve was obtained assuming that the thickness of a ZnO layer with quenched PL was 10 nm near every graphene/ZnO interface. However, as it can be seen in Figure 3.12.a, b, PL signals are still detected when the presumed total thickness of ZnO layers between the two graphene layers is 10 nm (see Figure 3.12.b, $G_{11L}ZnO_{10nm}$). Consequently, it can be concluded that PL quenching mechanism in the nanolaminates may not be only based on the dimensions of the nanostructure, and a more complex model is required to fully understand the optical properties of such G/ZnO nanolaminates.

3.3. Graphene/Bi_2Se_3/ZnO layered heterostructure for application in optoelectronic devices

3.3.1. Morphology of quartz/Bi_2Se_3/ZnO and graphene/Bi_2Se_3/ZnO heterostructures

The results of this chapter are described in the publication № 1.

Q/Bi_2Se_3/ZnO and G/Bi_2Se_3/ZnO heterostructures were fabricated by deposition of ZnO nanolayers of different thicknesses (from 10 to 150 nm) on top of the described in 3.1. chapter Bi_2Se_3 nanostructured coatings, consisting from the randomly oriented coalesced nanoplates on quartz (Q) substrate, and from the coalesced horizontally oriented nanoplates on graphene (G) substrate (Figure 3.1.b and Figure 3.2.b respectively).

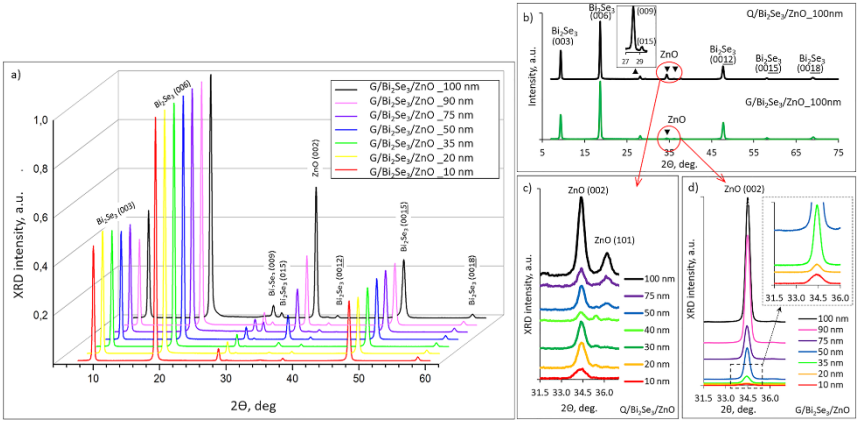

Figure 3.13. **Full XRD patterns of (a) G/Bi_2Se_3/ZnO heterostructures with ZnO nanolayers of thicknesses 10−100 nm, (b) G/Bi_2Se_3/ZnO (green) and Q/Bi_2Se_3/ZnO (black) heterostructures with ZnO nanolayer thickness of 100 nm, and (c, d) enlarged images of the region of ZnO diffraction plane positions for the Q/Bi_2Se_3/ZnO (c) and G/Bi_2Se_3/ZnO (d, including inset) heterostructures with the different ZnO nanolayer thicknesses**

In the XRD spectra of the obtained heterostructures (Figure 3.13.a, b), two diffraction peaks corresponding to ZnO crystallographic planes ((002) at 2Θ = 34.38° and (101) at 2Θ = 36.16°) were detected for Q/Bi_2Se_3/ZnO heterostructures and only one (corresponding to the (002) plane at 2Θ = 34.38°) was detected for G/Bi_2Se_3/ZnO heterostructures. The presence of the characteristic for ZnO diffraction peaks already in the XRD patterns obtained for 10 nm thick ZnO layers (Figure 3.13.c, d) indicates highly crystalline structure of 10−100 nm thin ZnO nanolayers in G/Bi_2Se_3/ZnO and Q/Bi_2Se_3/ZnO heterostructures and differs significantly from the ALD growth of ZnO on Si, which results in formation of polycrystalline thin films. In the latter case, two main diffraction peaks corresponding to (100) and (101) ZnO reflection planes and the transition from the amorphous (below 50 nm of thickness) states to the crystalline were observed [27].

The absence of the main (100) diffraction peak for Si/ZnO thin films in Q/Bi_2Se_3/ZnO XRD spectra indicates the similarity of the ZnO growth mechanism to that in G/Bi_2Se_3/ZnO heterostructures (growth in one direction). The lower intensities of the ZnO (002) reflection peak of Q/Bi_2Se_3/ZnO heterostructures in comparison with that of G/Bi_2Se_3/ZnO heterostructures, and the presence of the (101) reflection peak in the diffraction pattern of Q/Bi_2Se_3/ZnO may be explained by the morphology of the Q/Bi_2Se_3 substrate surface, promoting the growth of the ZnO nanolayers not only parallel to the quartz surface but also under different directions relative to it (on the surfaces of

the Bi_2Se_3 nanoplates oriented under different angles relative to the quartz substrate surface).

High-resolution TEM and FFT images (Figure 3.14.a-d) confirm the orientation of ZnO crystalline grains in different directions in the Q/Bi_2Se_3/ZnO heterostructure with the ZnO layer thickness of 50 nm. EDX analysis of the cross-section of the Q/Bi_2Se_3/ZnO heterostructure (Figure 3.14.e) revealed the presence of an approximately 8 nm thin transition layer at the Bi_2Se_3/ZnO interface.

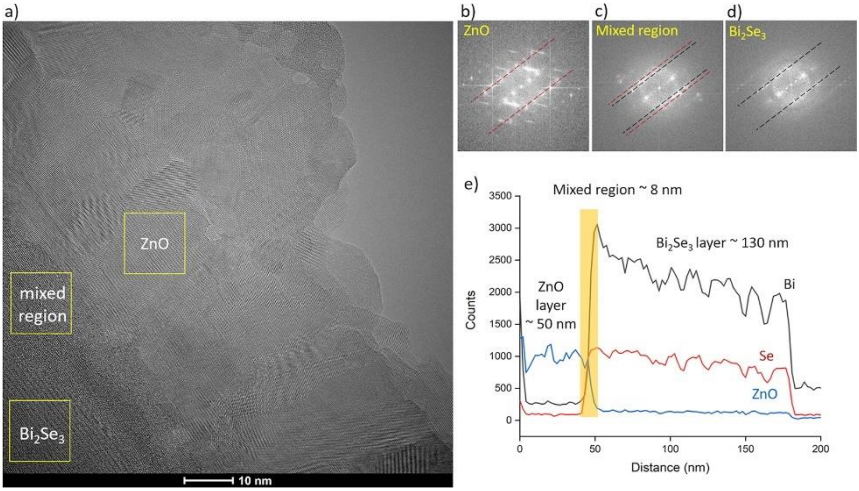

Figure 3.14. **(a) High-resolution TEM image of the cross-section of the Q/Bi_2Se_3/ZnO heterostructure with a ZnO nanolayer thickness 50 nm; (b-d) FFT images of ZnO, transition layer at the Bi_2Se_3/ZnO interface, and Bi_2Se_3, taken from the areas of the sample labeled with squares at the TEM image; (e) Line EDX scan of the cross-section of the Q /Bi_2Se_3/ZnO (50 nm) sample**

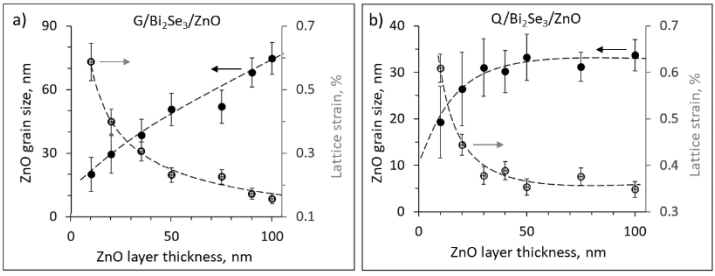

Figure 3.15. **Apparent ZnO grain size (primary y-axis, black circles) and lattice strain (secondary y-axis, hollow circles) vs ZnO nanolayer thickness in a) G/Bi_2Se_3/ZnO and b) Q/Bi_2Se_3/ZnO heterostructures**

Dependence of the ZnO crystalline grain sizes and crystal lattice strain effects, estimated from the XRD spectra, on the thickness of ZnO layers in Q/Bi_2Se_3/ZnO and G/Bi_2Se_3/ZnO heterostructures is shown in Figure 3.15. with the increase of ZnO nanolayer thickness, the G/Bi_2Se_3/ZnO heterostructures showed the nearly linear tendency of the increase of the average grain size accompanied by simultaneous decrease of the lattice strain. This indicates the improvement of the ZnO crystalline structure with the increase of ZnO nanolayer thickness. In contrast, for the Q/Bi_2Se_3/ZnO heterostructures an increase in grain size, accompanied by the decrease in the lattice strain was observed only for ZnO nanolayers thicknesses below 30 nm. Above this value, the average ZnO grain size in the Q/Bi_2Se_3/ZnO heterostructures is approximately 30 nm and is practically unchanged, which is consistent with the size of grains visible at the high-resolution TEM image (Figure 3.14.a). The smaller average size of the ZnO grains is probably related to the surface morphology of the Q/Bi_2Se_3 substrates, when ZnO samples growing on Bi_2Se_3 nanoplates of different orientations start to interfere with each other, thus hampering the formation of larger grain. Such a difference between the grain sizes in G/Bi_2Se_3/ZnO and Q/Bi_2Se_3/ZnO heterostructures may lead to a higher number of optically active defects in Q/Bi_2Se_3/ZnO heterostructures formed at the ZnO grain boundaries in comparison with that for G/Bi_2Se_3/ZnO heterostructures.

3.3.2. Optical properties of graphene/Bi_2Se_3/ZnO heterostructures

The results of this chapter are described in the publication № 1.

The band gap values determined from the absorption spectra of ZnO nanolayers varied from 3.21 to 3.27 eV and from 3.21 to 3.25 eV for in Q/Bi_2Se_3/ZnO heterostructures and G/Bi_2Se_3/ZnO heterostructures, respectively. These values are consistent with the optical band gap values reported previously for ZnO thin films on Si substrates (3.2 eV [27]) and are lower than the typical band gap value of a ZnO single crystal (3.37 eV [50]). Such redshift of the optical band gap of the ZnO nanolayers in Bi_2Se_3/ZnO heterostructures in comparison with the bulk ZnO (single ZnO crystal) may be related to a higher number of optically active point defects like Zn, O vacancies, and Zn interstitials formed in the ZnO nanolayer near the Bi_2Se_3/ZnO interface, as well as at the ZnO grain boundaries. These defects may form shallow states close to the conduction and valence band of ZnO [17, 27, 51-52], that would result in reduction of the band gap value in comparison to the bulk ZnO.

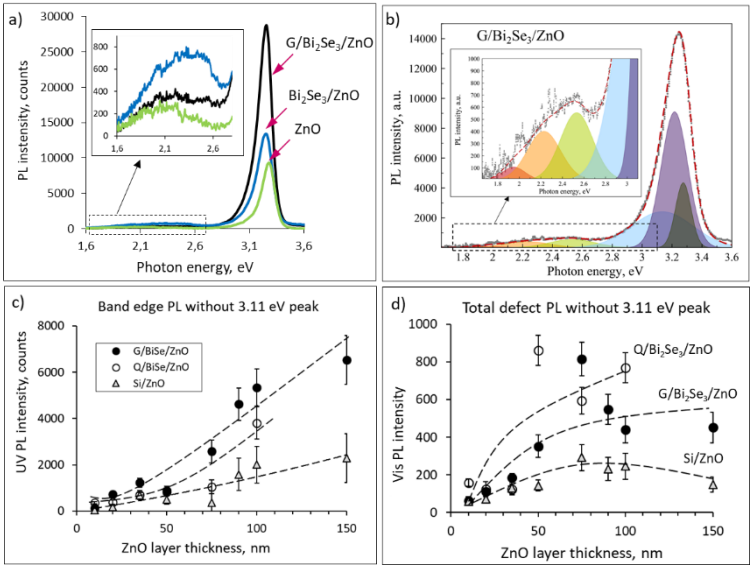

Figure 3.16. **a) Photoluminescence spectra of G/Bi_2Se_3/ZnO and Q/Bi_2Se_3/ZnO heterostructures and for the comparison of 100 nm ZnO thin film on Si; b) An example of a deconvoluted G/Bi_2Se_3/ZnO PL spectrum; Band edge PL intensities (c) and defect emission PL intensities (d) of G/Bi_2Se_3/ZnO, Q/Bi_2Se_3/ZnO and Si/ZnO vs ZnO nanolayer thickness (without the contribution of the 3.11 eV peak related to the neutral Zn vacancies)**

PL of the ZnO nanolayers in G/Bi_2Se_3/ZnO and Q/Bi_2Se_3/ZnO heterostructures was compared to the PL of the same thickness ALD ZnO thin films in Si/ZnO heterostructures. Generally, the PL spectra of all types of ZnO nanolayers exhibited two maxima (Figure 3.16.a): an intensive, narrow peak at ~3.2 eV and a broad peak centered at 2.3-2.4 eV. Deconvolution of the PL spectra performed by Gaussian fitting (Figure 3.16.b) revealed the presence of two PL peaks centered at 3.24 eV and 3.30 eV, which can be related to the ZnO band-edge emission, and four PL peaks that can be related to the charge carrier recombination on different types of defects, such as neutral zinc interstitials (peak centered at ~3.11 eV), singly ionized oxygen and zinc vacancies (peak centered at ~2.5 eV), double ionized oxygen vacancies (peak centered at (~2.23 eV), and oxygen interstitials (peaks centered at ~1.96 eV) [25, 53]. As can be seen from Figure 3.16.b, the emission peak related to the neutral zinc interstitials (~3.11 eV) is significantly contributing to the total intensities of both maxima of the PL spectra. Traditionally, the influence of this peak is not separated from the summarized intensities of the band-edge and visible defect PL peaks of ZnO. In this work, the contribution of the defect emission peak centered at ~3.11 eV is

removed from the total intensities of PL peaks in order to analyse the dynamics of the PL band components. Further analysis of PL intensities was based on intensities of the peaks centred at 3.24 and 3.3 eV for band-edge PL and on the peaks centred at ~1.96, ~2.23 un ~2.5 eV for defect emission PL.

The intensity of the band-edge PL of ZnO excitons in G/Bi_2Se_3/ZnO and Q/Bi_2Se_3/ZnO heterostructures for all ZnO nanolayer thicknesses was found to be significantly higher in comparison with the Si/ZnO heterostructures (~3.3 and ~1.7 times, respectively, Figure 3.16.c). Such enhancement of the band-edge PL of ZnO may be a result of the superposition of several mechanisms: (1) charge transfer between the Bi_2Se_3 and ZnO nanolayers; (2) improvement of crystalline structure of ZnO during the growth; (3) coupling of the band-edge excitons with the surface-plasmon polaritons.

In contrast with the Si/ZnO deposited on p-doped Si substrates, where the depleted regions are formed near to the interface in both Si and ZnO, the joining of ZnO and Bi_2Se_3 in a heterostructure results in formation of the electron-rich and hole-rich areas in ZnO and Bi_2Se_3, respectively. Forming the hole-rich region in Bi_2Se_3 results in a decrease of the electron concentration in this material [6]. Forming the electron-rich area in ZnO reduces the depletion layer formed at the surface of ZnO due to the chemisorption of oxygen [17, 54-55]. Reduction of the depletion layer of ZnO due to formation of the Bi_2Se_3/ZnO heterojunction will lead to an increase of the band-edge PL of ZnO in comparison with the ZnO of the same thickness, deposited on p-doped Si substrates.

However, the equal decrease of the ZnO depleted layer for both types of heterostructures does not explain the significantly higher band-edge PL of the ZnO in G/Bi_2Se_3/ZnO heterostructures in comparison with the band-edge PL of the ZnO in Q/Bi_2Se_3/ZnO heterostructures (Fig. Figure 3.16.a, c). This difference may be the result of other mechanisms.

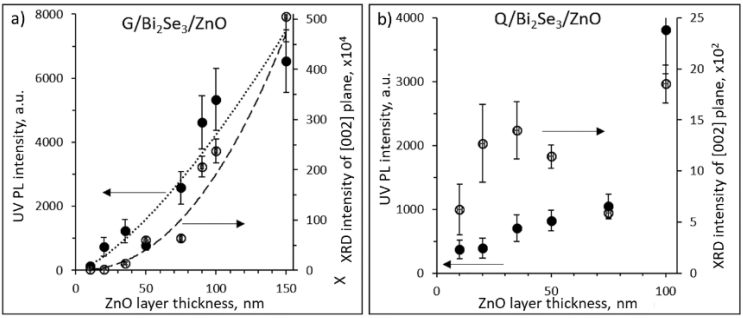

Figure 3.17. **Dependence of ZnO photoluminescence intensity (primary y-axis, black circles, dotted line) and XRD peak intensity (secondary y-axis, hollow circles, dashed line) on ZnO layer thickness of (a) G/Bi_2Se_3/ZnO and (b) Q/Bi_2Se_3/ZnO heterostructures**

Figure 3.17 illustrates the correlation between the intensity of the XRD peak related to the ZnO (002) reflection plane and the intensity of the band-edge PL emission of ZnO in Bi_2Se_3/ZnO heterostructures. The increase of the intensities of the XRD and the band-edge PL peaks with the increase of the ZnO thickness for the ZnO nanolayers in G/Bi_2Se_3/ZnO heterostructures is in line with the data related to the ZnO grain sizes and proves that the improvement of the crystalline structure of the ZnO is one of the mechanisms for the band-edge PL enhancement (Figure 3.17.a and 3.15.a). On the other hand, for Q/Bi_2Se_3/ZnO heterostructures such a correlation between the values of intensities of XRD and band-edge PL is not obvious (Figure 3.17.b and 3.15.b). Presumably, in this case, the ZnO crystallinity improvement is not the dominating mechanism for the band-edge PL enhancement. This conclusion is supported by the data shown in Figure 3.15.b, demonstrating no increase of the ZnO grain size in Q/Bi_2Se_3/ZnO heterostructures with the increase in the thickness of the ZnO nanolayer.

However, the larger increase of the ZnO PL in the G/Bi_2Se_3/ZnO and Q/Bi_2Se_3/ZnO heterostructures in comparison with the increase of the intensity of the XRD peak (Figure 3.17) may indicate the influence of the third mechanism of the PL enhancement. It could be related to the combination of ZnO excitons with Bi_2Se_3 surface plasmon polaritons following a similar mechanism described in [18], where mechanically exfoliated flakes of another topological insulator Bi_2Te_3 with a thickness below 200 nm were placed on the ZnO surface.

In contrast to the band-edge luminescence, the most intense defect-related PL is detected for the Q/Bi_2Se_3/ZnO heterostructures (6 times higher in comparison with the defect-related PL intensity of Si/ZnO structures, Figure 3.16.d). The defect PL intensity of the nanolayers of G/Bi_2Se_3/ZnO heterostructures was 1.5-3 times higher in comparison with the Si/ZnO heterostructures, and showed linear increase with the increase of the ZnO nanolayer thickness. Presumably, this enhancement of the defect ZnO PL in Bi_2Se_3/ZnO heterostructures is promoted by the decrease of the depletion layer in comparison to the ZnO films deposited on Si substrates [17, 27]. The significantly higher defect PL of ZnO in Q/Bi_2Se_3/ZnO heterostructures in comparison with G/Bi_2Se_3/ZnO heterostructures may be explained by the differences in the surface morphology and smaller ZnO grain sizes, resulting in a larger area of grain boundaries. The defect PL increase can be related to the higher concentration of the single-ionized oxygen and zinc vacancies (~ 2.5 eV) in Q/Bi_2Se_3/ZnO samples. As it is known, these defects are concentrated on the ZnO grain boundaries.

CONCLUSIONS

1. In the synthesis of Bi_2Se_3 nanostructures by the catalyst-free physical vapor deposition method, the use of carrier gas flow during the certain temperature region of the cooling stage promotes rapid increase of concentration of the vaporised source material delivered to the substrate and causes the temperature gradient across nanoplates, thus shifting the growth direction of the nanostructures towards the other main crystallographic growth directions. Thus, it is possible to obtain monocrystalline nanostructures of stoichiometric Bi_2Se_3 of different morphology – nanoplates, nanoribbons and nanostructured coatings consisting from the nanoplates oriented in one or in different directions – on different substrates.

2. The Bi_2Se_3 nanostructured coating on graphene, consisting from nanoplates oriented at different angles relative to the substrate surface, exhibited 1.5 and 2 times enhanced thermoelectric response to the direct thermal exposure and infrared radiation, respectively, indicating that it can be useful for applications in thermoelectric and photodetection devices.

3. A method for the synthesis of multilayer nanostructures - graphene/ZnO nanolaminates - with precisely controlled composition and interlayer thickness is developed. Graphene interlayers contribute to the formation of ZnO crystalline structure and to the photoinduced electron transfer. The resulting dependence of ZnO photoluminescence and graphene charging on the number of graphene layers in nanolaminates, as well as on the thickness of ZnO interlayers can be used in the development of optical sensors.

4. In comparison with the Bi_2Se_3/ZnO heterostructures grown on quartz and ZnO thin films grown on silicon, the use of graphene substrate for the synthesis of Bi_2Se_3/ZnO heterostructures improves the crystalline structure of Bi_2Se_3 and ZnO, and significantly increases the ZnO luminescence intensity. The increase of the photoluminescence intensity of Bi_2Se_3/ZnO heterostructures is related to: 1) the decrease of the depletion layer due to the charge transfer at the Bi_2Se_3/ZnO interface and the formation of hole-rich and electron-rich regions in Bi_2Se_3 and ZnO, respectively; 2) the improvement of the ZnO crystallinity, especially in the Bi_2Se_3/ZnO heterostructures on graphene; 3) the resonance of ZnO excitons with the Bi_2Se_3 surface plasmon polaritons at the Bi_2Se_3/ZnO interface.

REFERENCES

[1] Mishra, S.K.; Satpathy, S.; Jespen, O. Electronic structure and thermoelectric properties of bismuth telluride and bismuth selenide. *J. Phys. Condens. Matter*, **1997**, *9*, 461-470

[2] Zhang, H.; Liu, C.-X.; Qi, X.-L.; Dai, X.; Fang, Z.; Zhang, S.-C. Topological insulators in Bi_2Se_3, Bi_2Te_3 and Sb_2Te_3 with a single Dirac cone on the surface. *Nat. Phys.*, **2009**, *5*, 438-442

[3] Kosmaca, J.; Jasulaneca, L.; Meija R.; Andzane, J.; Romanova, M.; Kunakova, G.; Erts, D. Young's modulus and indirect morphological analysis of Bi_2Se_3 nanoribbons by resonance measurements. *Nanotechnology*, **2017**, 28, 325701

[4] Dang, W.; Peng, H.; Li, H.; Wang, P.; Liu, Z. Epitaxial heterostructures of ultrathin topological insulator nanoplateand graphene. *Nano Lett.* **2010**, *10*, 2870

[5] Raghu, S.; Chung, S. B.; Qi, X.-L.; Zhang, S.-C. Collective modes of a helical liquid. *Phys. Rev. Lett.*, **2010**, *104*, 116401

[6] Hong, S. S.; Cha, J. J.; Kong, D.; Cui, Y. Ultra-low carrier concentration and surface-dominant transport in antimony-doped Bi_2Se_3 topological insulator nanoribbons. *Nat. Commun.*, **2012**, *3*, 757

[7] Tereshchenko, A.; Bechelany, M.; Viter, R.; Khranoyskyy, V.; Smyntyna, V.; Starodub, N.; Yakimova, R. Optical biosensors based on ZnO nanostructures: advantages and perspectives. A review. *Sens. Actuators B*, **2016**, *229*, 664

[8] Nazareth, V. Thin-film single-walled carbon nanotube transistors fabricated using mechanical meniscus aligned arrays. *Materials Science* **2012**.

[9] Biroju, R.K.; Tilak, N.; Rajender, G.; Dhara, S.; Giri, P.K. Catalyst free growth of ZnO nanowires on graphene and graphite oxide and its enhanced photoluminescence and photoresponce. *Nanotechnology* **2015**, *26*, 145601

[10] Dutta, M.; Sarkar, S.; Ghosh, T.; Basak, D. ZnO/Graphene quantum dot solid-state solar cell. *J. Phys. Chem. C.* **2012**, *116*, 20127

[11] Liu, F.; Zhang, Y.; Yu, J.; Wang, S.; Ge, S.; Song, X. Application of ZnO/Graphene and S6 Aptamers for Sensitive Photoelectrochemical Detection of SK-BR-3 Breast Cancer Cells Based on a Disposable Indium Tin Oxide Device. *Biosens. Bioelectron.* **2014**, *51*, 413

[12] Geim, K. A.; Novoselov, S. K. Graphene. Scientific background on the nobel prize in physics 2010. The Royal Swedish Academy of Sciences, **2010**. https://www.nobelprize.org/uploads/2018/06/advanced-physicsprize2010.pdf [skatīts 26.08.2021]

[13] Pearsall T.P. *Strained-layer superlattices: Materials science and technology. Semiconductors and semimetals*. Vol. 33. Acedemic Press, Inc.: New York, **1991**, 443

[14] Ozgur, U.; Alivov, Y. I.; Liu, C.; Teke, A.; Reshchikov, M. A.; Dogan, S.; Avrutin, V.; Cho, S. J.; Morkoc, H. A comprehensive review of ZnO materials and devices. *J. Appl. Phys.* **2005**, *98*, 41301

[15] Jiao, K.; Wu, X.; Duan, C.; Zhang, D.; Wang, Y.; Chen, Y. Novel ALD-assisted growth of ZnO nanorods on graphene and its $Cu_2ZnSn(S_xSe_{1-x})$ solar cell application. *Phys. Chem. Chem. Phys.* **2015**, *17*, 4757

[16] Zhang, H.; Babichev, A. V.; Jacopin, G.; Lavenus, P.; Julien, F. H.; Egorov Y. A.; Zhang, J.; Pauporte, T.; Tchernycheva, M. Characterization and modeling of a ZnO nanowire ultraviolet photodetector with graphene transparent contact. *J. Appl. Phys.* **2013**, *114*, 234505

[17] Chaaya, A. A.; Viter, R.; Baleviciute, I.; Bechelany, M.; Ramanavicius, A.; Gertnere, Z.; Erts, D.; Smyntyna, V.; Miele P. Tuning optical properties of Al_2O_3/ZnO nanolaminates synthesized by atomic layer deposition. *J. Phys. Chem. C.* **2014**, *118*, 3811

[18] Laio, Z.-M.; Han B.-H.; Wu, H.-C.; Yashina, L. V.; Yan, Y.; Zhou, Y.-B.; Bie, Y.-Q.; Bozhko, S. I.; Fleischer. K.; Shvets, I. V.; Zhao, Q.; Yu, D.-P. Surface plasmon on topological insulator/dielectric interface enhanced ZnO ultraviolet photoluminescence. *AIP Adv.*, **2012**, *2*, 022105

[19] Singh, V.; Joung, D.; Zhai, L.; Das, S.; Khondaker, S.I.; Seal, S. Graphene based materials: past, present and future. *Progress in Materials Science* **2011**, *56*, 1178

[20] Kumar, A.; Lee, C.H. Synthesis and biomedical applications of graphene: present and future trends. *Advances in Graphene Science* **2013**, 5772-5578, DOI: 10.5772/55728

[21] Kumar, K.; Kim, Y.; Yang, E. The influence of thermal annealing to remove polymeric residue on the electronic doping and morphological characteristics of graphene. *Carbon* **2013**, *65*, 35

[22] Mlack, J.T.; Rahman, A.; Johns, G.L.; Livi, K.J.; Markovic, N. Substrate-independent catalyst-free synthesis of high-purity Bi_2Se_3 nanostructures. *Appl. Phys. Lett.* **2013**, *102*, 193108

[23] Hamdou, B.; Kimling, J.; Dorn, A.; Pippel, E.; Rostek, R.; Woias, P.; Nielsch, K. Thermoelectric characterization of bismuth telluride nanowires, synthesized via catalytic growth and post-annealing. *Adv. Mater.* **2013**, *25*, 239

[24] Schonherr, P.; Zhang, F.; Kojda, D.; Mitdank, R.; Albrecht, M.; Fischer, S.F.; Hesjeda, T. Free-standing millimetre-long Bi_2Te_3 sub-micron belts catalyzed by TiO_2 nanoparticles. *Nanoscale Res. Lett.* **2016**, *11*, 308

[25] Eliasa, J.; Bechelany, M.; Utke, I.; Erni, R.; Hosseini, D.; Johann, Michler J.; Philippea, L. Urchin-inspired zinc oxide as building blocks for nanostructured solar cells. *Nano Energy* **2012**, *1*, 696

[26] Yu, M.; Wang, A.; Wang, Y.; Li, C.; Shi, G. An alumina stabilized ZnO–graphene anode for lithium ion batteries via atomic layer deposition. *Nanoscale* **2014**, *6*, 11419

[27] Chaaya A. A.; Viter, R.; Bechelany, M.; Alute, Z.; Erts, D.; Zalesskaya, A.; Kovalevskis, K.; Rouessac, V.; Miele, P. Evolution of microstructure and related optical properties of ZnO grown by atomic layer deposition. *Beilsten J. Nanotechnol.* **2013**, *4*, 690

[28] Mattevi, C.; Kim, H.; Chhowalla, M. A review of chemical vapour deposition of graphene on copper. *J. Mater. Chem.* **2011**, *21*, 3324

[29] Ghoneim, M. T.; Smith, C. E.; Hussain, M. M. Simplistic graphene transfer process and its impact on contact resistance. *Appl. Phys. Lett.* **2013**, *102*, 183115

[30] Scan line profile determined by the tip shape. Micro Cantilevers. Olympus Corporation, **2018**. http://probe.olympus-global.com/en/product/scanprfl.html [skatīts 03.01.2022]

[31] Sondors, R.; Kunakova, G.; Jasulaneca, L.; Andzane, J.; Kauranens, E.; Bechelany, M.; Erts, D. High-yield growth and tunable morphology of Bi_2Se_3 nanoribons synthesized on thermally dewetted Au. *Nanomaterials* **2021**, *11*, 2020

[32] Song M. S., Choi S.B., Kim Y. Wurtzite ZnTe nanotrees and nanowires on fluorine-doped tin oxides glass substrates. Nano Lett. **2017**, *17*, 4365

[33] Tu, F.; Xie, J.; Cao, G.; Zhao, X. Self-assembly of Bi_2Te_3-nanoplate/graphene-nanosheet hybrid by one-pot route and its improved Li-storage properties. *Materials*, **2012,** *5*, 1275-1284

[34] Kong, D.; Cha, J.J.; Lai, K.; Peng, H.; Analytis, J.G. Rapid surface oxidation as a source of surface degradation factor for Bi2Se3. *ACS Nano* **2011**, *5*, 4698

[35] Morris, M.C.; Murdie H.F.; Evans, E.H.; Paretzkin, B.; Parker, H.S.; Panagiotopoulos, N.C. *Standard X-ray diffraction powder patterns*. Nat. Bur. Stand., Washington **1981**

[36] Sun, Z.; Liufu S.; Liu, R.; Chen, X.; Chen L. A general strategy to bismuth chalcogenide films by chemical vapor transport. *J. Mater. Chem.* **2011**, *21*, 2351

[37] Klingshirn, C. Introduction. *Zinc Oxide: From Fundamental Properties Towards Novel Applications.* Springer: Berlin, Heidelberg, **2010**, 1-6

[38] Si, C.; Sun, Z.; Liu, F. Strain engineering of graphene: a review. *Nanoscale* **2016**, *8*, 3207

[39] Malard, L. M.; Pimenta, M. A.; Dresselhaus, G.; Dresselhaus, M. S. Raman spectroscopy in graphene. *Phys. Rep.* **2009**, *473*, 51

[40] Kudin, K. N.; Ozbas, B.; Schniepp, H. C.; Prud'homme R. K.; Aksay, I. A.; Car, R. Raman spectra of graphite oxide and functionalized graphene sheets. *Nano Lett.* **2008**, *8*, 36

[41] Wu, W.; Yu, Q.; Peng, P.; Liu, Z.; Bao, J.; Pei, S.-S. Control of thickness uniformity and grain size in graphene films for transparent conductive electrodes. *Nanotechnology* **2012**, *23*, 35603

[42] Luo, Z.; Lu, Y.; Singer, D. W.; Berck, M. E.; Somers, L. A.; Goldsmith, B. R.; Johnson, A. T. C. Effect of substrate roughness and feedstock concentration on growth of wafer-scale graphene at atmospheric pressure. *Chem. Mater.* **2011**, *23*, 1441

[43] Shin, K.-S.; Jo, H.; Shin, H.-J.; Choi, W. M.; Choi, J.-Y.; Kim, S.-W. High quality graphene-semiconducting oxide heterostructure for inverted organic photovoltaics. *J. Mater. Chem.* **2012**, *22*, 13032

[44] Beams, R.; Cancado, L. G.; Novotny, L. Raman characterization of defects and dopants in graphene. *J. Phys. Condens. Matter.* **2015**, *27*, 83002

[45] Iqbal, M. W.; Iqbal, M. Z.; Khan, M. F.; Jin, X.; Hwang, C.; Eom, J. Modification of the structural and electrical properties of graphene Layers by Pt Adsorbates. *Sci. Technol. Adv. Mater.* **2014**, *15*, 55002

[46] Viter, R.; Chaaya A. A.; Iatsunskyi, I.; Nowaczyk, G.; Kovalevskis, K.; Erts, D.; Miele, P.; Smyntyna, V.; Bechelany, M. Tuning of ZnO 1D nanostructures by atomic layer deposition and electrospinning for optical gas sensor applications. *Nanotechnology* **2015**, *26*, 105501

[47] Ozerov, I.; Arab, M.; Safarov, V. I.; Marine, W.; Giorgio, S.; Sentis, M.; Nanai, L. Enhancement of exciton emission from ZnO nanocrystalline films by pulsed laser annealing. *Appl. Surf. Sci.* **2004**, *226*, 242

[48] Reynolds, D. C.; Look, D. C.; Jogai, B.; Collins, T. C. Polariton and free-exciton-like photoluminescence in ZnO. *Appl. Phys. Lett.* **2001**, *79*, 3794

[49] Xu, P.; Tang, Q.; Zhou, Z. Structural and electronic properties of graphene-ZnO interfaces: dispersion-corrected density functional theory investigations. *Nanotechnology* **2013**, *24*, 305401

[50] Liang, W. Y.; Yoffe, A. D. Transmission spectra of ZnO single crystals. *Phys. Rev. Lett.* **1968**, *20*, 59

[51] Arif, A.; Belahssen, O.; Gareh, S.; Benramache, S. The calculation of band gap energy in zinc oxide films. *J. Semicond.* **2015**, *36*, 013001

[52] Fang, J.; Fan, H.; Ma, Y.; Wang, Z.; Chang, Q. Surface defects control for ZnO nanorods synthesized by quenching and their anti-recombination in photocatalysis. *Appl. Surf. Sci.* **2015**, *332*, 47

[53] Janotti, A.; Van De Walle, C. G. Native point defects in ZnO. *Phys. Rev. B: Condens. Matter Mater. Phys.* **2007**, *76*, 165202

[54] Viter, R.; Iatsunskyi, I.; Fedorenko, V.; Tumenas, S.; Balevicius, Z.; Ramanavicius, A.; Balme, S.; Kempiński, M.; Nowaczyk, G.; Jurga, S.; et al. Enhancement of electronic and optical properties of ZnO/Al_2O_3 nanolaminate coated electrospun nanofibers. *J. Phys. Chem. C* **2016**, *120*, 5124

[55] Reshchikov, M. A.; Behrends, A.; Bakin, A.; Waag, A. Photoluminescence from ZnO nanowires. *J. Vac. Sci. Technol. B Microelectron. Nanom. Struct.* **2009**, *27*, 1688

ACKNOWLEDGMENTS

I express my gratitude to my supervisor, prof. Donats Erts for his support during the creation of the doctoral thesis, for the opportunity to study such a unique material - graphene. Thank you for the opportunity to be in progress - to learn new synthesis methods, learn to work on complex equipment, the opportunity to gain experience in the field of nanotechnology both here in Latvia and abroad.

I would like to thank all my colleagues from the Institute of Chemical Physics of the University of Latvia. Many thanks to Dr. Jana Andzane for the creative ideas, provided consultations, for the help with the experiments and interpretation of results, for the support and training in the writing of influential publications. Special thanks to Dr. Raimonds Poplausks, Dr. Raimonds Meija, Dr. Marina Romanova for the help with measurements and Dr. Juris Katkevics, Dr. Jelena Kosmaca, Dr. Juris Prikulis, Dr. Irina Olisevica, Daniels Jevdokimovs, Andris Lescinskis, Uldis Malinovskis, Lasma Bugovecka, Edgar Mamis, Ingus Andersons and Gvido Petersons for discussions and great emotional support during the creation of the thesis.

I express my gratitude to Dr. Roman Viter from the Institute of Atomic Physics and Spectroscopy of the University of Latvia and Dr. Igor Iatsunskyi from the NanoBiomedicine Center in Poland for their collaboration, discussions and help in the explanation of the measurement results.

I would like to thank Dr. Mikhael Bechelany from the European Membrane Institute of the University of Montpellier for the opportunity to gain experience and develop part of the thesis in his scientific group. I would like to thank the ERASMUS+practice program and the Latvian-French partnership project "OSMOSIS" for the financial support and the opportunity to participate in this exchange. I would like to thank the staff of the European Insitute of Membranes for the friendly and nice communication during my ERASMUS traineeship. Special thanks to Dr. Viktoriia Fedorenko, Dr. Matthew Weber and Dr. Octavio Graniel for help in working with the ALD reactor.

I would like to thank the University of Latvia, the European Social Fund, and the European Regional Development Fund for scholarships and financial support. I would like to thank L'Oreal Baltic for the scholarship "Women in science" with the support of the Latvian National Commission of UNESCO and the Latvian Academy of Sciences.

Finally, I would like to express my special thanks to my family. Thank you for your support and understanding when the light was on and the keyboard clicked at night.